Surrogate-Assisted Bayesian Inference of Fracture Network Parameters from Elastic Waves: A Sensitivity-Guided Approach

Le Zhang[1,2*], Qinghua Lei[3], Longjun Dong[4], Chuanyin Jiang[3], Thomas Hermans[1]

[1] Department of Geology, Ghent University, Ghent, Belgium
[2] Faculty of Civil Engineering and Geosciences, Delft University of Technology, Delft, The Netherlands
[3] Department of Earth Sciences, Uppsala University, Uppsala, Sweden
[4] School of Resources and Safety Engineering, Central South University, Changsha, China

[*] Corresponding author: le.zhang@ugent.be

Submission Statement

This is a non-peer-reviewed preprint submitted to *EarthArXiv*.
This manuscript has been submitted for peer review to
Journal of Geophysical Research: Machine Learning and Computation.

Surrogate-Assisted Bayesian Inference of Fracture Network Parameters from Elastic Waves: A Sensitivity-Guided Approach

Le Zhang[1,2*], Qinghua Lei[3], Longjun Dong[4], Chuanyin Jiang[3], Thomas Hermans[1]

[1]Department of Geology, Ghent University, Ghent, Belgium
[2]Faculty of Civil Engineering and Geosciences, Delft University of Technology, Delft, The Netherlands
[3]Department of Earth Sciences, Uppsala University, Uppsala, Sweden
[4]School of Resources and Safety Engineering, Central South University, Changsha, China

Key Points:

- Inverse Q and normalized transmitted energy capture fracture-stiffness effects on wave transport from propagation to diffusion/localization.
- DGSA ranks how dimensionless stiffness, fracture density, percolation, and power-law exponent control the two wave-transport metrics.
- Stiffness is best identified in propagation and superdiffusion, while density and connectivity are best constrained near normal diffusion.

Corresponding author: Le Zhang, le.zhang@ugent.be

Abstract

We develop a sensitivity-guided, surrogate-assisted Bayesian framework to infer fracture network parameters from elastic waves. Synthetic fracture networks characterized by power-law length exponent a, fracture density d, and percolation parameter p are constructed. Elastic wave propagation through these fracture networks is then simulated across a range of dimensionless specific stiffness values $\tilde{\kappa}$. From 2560 Monte Carlo simulation runs, we extract two wave transport metrics: the inverse quality factor Q^{-1} and the normalized transmitted energy E. Distance-based generalized sensitivity analysis in the (Q^{-1}, E) space reveals stiffness-dependent wave transport regimes (propagation, superdiffusion, normal diffusion, subdiffusion, and localization) and quantifies the contributions of parameters a, d, p and $\tilde{\kappa}$ in each regime. A random forest surrogate for the mapping of $(a, d, p, \tilde{\kappa}) \mapsto (Q^{-1}, E)$ is then embedded in a Metropolis-Hastings scheme to perform Bayesian inversion of fracture network parameters. When the dimensionless stiffness $\tilde{\kappa}$ is near 1, both a and d are reliably recovered, with posterior probabilities for the true values well above their uniform priors. For large $\tilde{\kappa}$ (corresponding to the propagation and superdiffusion regimes), the fracture stiffness itself becomes highly identifiable, and complementary inversions in which $\tilde{\kappa}$ is treated as unknown show that it can be robustly recovered from (Q^{-1}, E) in these regimes. For small $\tilde{\kappa}$ (subdiffusion and localization regimes), multiple scattering prevails and all parameters become more weakly resolved. Our results demonstrate that wave attenuation and energy metrics can be used to jointly invert fracture stiffness and network geometry, provided that the inversion targets wavefield regimes where these parameters are most sensitive.

Plain Language Summary

Fractures in rocks are important in many subsurface problems, from geothermal energy production and hydrocarbon recovery to underground energy storage, carbon sequestration, and nuclear waste disposal. Yet it is difficult to determine properties such as fracture density, connectivity, and stiffness from seismic waves, because the inversion is non-unique: different fracture patterns can produce very similar seismic signals. In this study, we generate many synthetic fracture networks, simulate elastic-wave propagation, and measure two simple quantities from synthetic seismograms: amplitude attenuation and transmitted energy over time. We use distance-based sensitivity analysis to identify which fracture properties most strongly control these metrics across wavefield regimes, from propagation to diffusion and localization. We then replace expensive wave simulations with a fast surrogate model and combine it with Bayesian inference to estimate fracture properties from the two metrics. We show that fracture stiffness is best constrained when fractures are neither extremely stiff nor extremely soft, and that fracture density and connectivity can also be inferred in favorable regimes. These results provide guidance for designing and interpreting seismic surveys in fractured rock.

1 Introduction

Fractures are widespread in crustal rocks and strongly influence the thermo-hydro-mechanical behavior of geological media. They play a key role in many geoscience and geoengineering applications, including hydrocarbon and geothermal production, groundwater management, CO_2 and H_2 storage, underground construction, and nuclear waste disposal (Tsang, 1999; Viswanathan et al., 2022). However, quantitative characterization of fracture systems remains difficult owing to their subsurface nature, limited observational data, strong scale dependence of their properties, and pronounced geometric heterogeneity across scales (Bonnet et al., 2001; Bour et al., 2002; Lei & Gao, 2018; Lei et al., 2015). Geophysical observations provide a practical means of probing fracture networks at reservoir scale, but inferring properties such as stiffness, density, and connectivity from these data is often strongly underdetermined, since different combinations of fracture stiffness and network geometry can produce very similar effective velocities, attenuation, and other geophysical

responses (Barbosa et al., 2019; Germán Rubino et al., 2013, 2014). This non-uniqueness motivates the development of methods that not only fit a particular data set, but also assess which fracture network parameters are resolvable from the available observations and under which conditions.

The elastic response of a fracture is governed by its normal and shear stiffnesses (Pyrak-Nolte, 1996; Pyrak-Nolte et al., 1990). For seismic waves with wavelengths much larger than the fracture size, the fracture behaves as a non-welded interface that modifies transmitted and reflected waves, affecting their amplitudes, phases, dispersion, and attenuation (Pyrak-Nolte et al., 1990; Schoenberg, 1980). Transmission and reflection coefficients as well as the seismic quality factor Q across a single fracture vary systematically with the fracture stiffness, as predicted by the displacement-discontinuity model and confirmed by laboratory observations (Pyrak-Nolte, 1996; Pyrak-Nolte & Cook, 1987; Pyrak-Nolte & Nolte, 1995; Pyrak-Nolte et al., 1992). These studies provide a quantitative basis for using seismic measurements to infer fracture stiffness. At the network scale, fracture systems can be described by parameters such as fracture density, orientation, length distribution, and connectivity, which often control large-scale rock mass properties such as equivalent permeability and bulk modulus (Berkowitz, 2002; Darcel et al., 2003; Davy et al., 2010; Lei & Gao, 2018). Early theoretical studies analyzed the seismic response of fractured media using effective medium approaches that idealize fractures as small, flat inclusions in an elastic solid and derive analytical expressions for effective stiffness, wave speeds, and attenuation as functions of fracture density, aspect ratio, and orientation under long-wavelength conditions (J. Hudson et al., 1996, 1997; J. A. Hudson & Liu, 1999). These models provide forward relationships between fracture network parameters and seismic wave properties. However, the fractal nature of natural fracture systems suggests that a representative elementary volume may not exist, challenging the applicability of effective medium approaches. Numerical simulations of wave propagation in discrete or stochastic fracture networks further showed that attenuation and velocity dispersion depend strongly on fracture connectivity, length distribution, and often exhibit behavior (e.g., anomalous diffusion, Anderson localization, nonlinear attenuation-frequency scaling) that departs from effective medium theory (Germán Rubino et al., 2013; Hunziker et al., 2018; Lei & Sornette, 2021, 2022).

Seismic data are used in many ways to estimate fracture network properties in the Earth's crust. Azimuthal amplitude and anisotropy analyses, as well as studies of frequency-dependent anisotropy, are used to infer fracture orientation, density, size distributions, and fluid fill (Baird et al., 2013; Maultzsch et al., 2003). These approaches fit effective medium or rock physics models to vertical seismic profiling, surface seismic, and microseismic data. Attenuation-based inversions and full-waveform inversion use measured amplitude decay and full waveforms to recover fracture compliance and effective stiffness, but typically rely on strong prior assumptions, dense acquisition, and substantial computational resources (Virieux & Operto, 2009; K. Wang et al., 2021; Yang et al., 2020). Another line of work uses fault zone head and trapped waves, and ambient noise-based methods, to image low-velocity cores, damage zones, and attenuation structure along major faults (Ben-Zion, 1998; Ben-Zion & Malin, 1991; Ben-Zion et al., 2003; Hillers et al., 2014). Despite these efforts, inferring fracture network properties from seismic data remains difficult. Different combinations of fracture density, length and aperture distributions, connectivity, and interfacial stiffness may produce similar effective velocities, anisotropy, and attenuation, while seismic data are confined to a limited frequency band, affected by noise, and recorded with incomplete source-receiver coverage (Ali & Jakobsen, 2011; Barbosa et al., 2019; Lewis & Ben-Zion, 2010). As a result, most existing inversions resolve only a small set of effective properties or rely heavily on assumed network architectures. This highlights the need for approaches that identify which fracture network parameters can be resolved from seismic data, and then leverage this knowledge to develop more targeted and well-posed inversion strategies.

Global sensitivity analysis provides a systematic way to examine how variations in parameters are reflected in system responses and to quantify the strength of their influence

on the observables. Distance-based generalized sensitivity analysis (DGSA) is an efficient, clustering-based variant that compares unconditional and cluster-conditional empirical cumulative distributions of the inputs, and has been applied in geoscientific problems such as geothermal reservoirs, hydrocarbon fields, groundwater resources, and solute transport (Park et al., 2016; Scheidt et al., 2018; Tas, Caers, & Hermans, 2025). When such analyses indicate that certain parameters exert a strong influence on the system responses, Bayesian inversion can be used to infer those parameters from data. However, its application is often limited by the computational cost of repeated simulations for complex forward models (Smith & Marshall, 2008). To reduce this cost, surrogate models based on machine learning are often embedded in Bayesian workflows to approximate expensive simulators and make sampling more efficient (Xu et al., 2017; J. Zhang et al., 2020). Their role in such workflows is primarily computational: they provide an efficient approximation of the forward model while leaving the physical modeling and Bayesian inference framework conceptually unchanged.

In this study, we propose a sensitivity-guided, surrogate-assisted Bayesian inversion framework for quantitative characterization of fracture networks. We first quantify the sensitivity of different fracture network parameters with respect to attenuation Q^{-1} and normalized energy E, and then use these sensitivity results to design the Bayesian inversion and improve its performance. Section 2 describes the numerical modeling of elastic wave propagation through synthetic fracture networks, the extraction of attenuation and energy metrics from the simulated wavefields, and a distance-based generalized sensitivity analysis combined with surrogate modeling and a Metropolis–Hastings Markov chain Monte Carlo scheme for Bayesian inversion. Section 3 presents forward-modeling results, global sensitivity patterns, and inversion results. Section 4 discusses parameter sensitivity and identifiability, evaluates the performance and limitations of the inversion framework, and outlines implications and outlook for applications to more realistic models and field data. Section 5 summarizes the main findings of the paper.

2 Methods

2.1 Governing Equations

The equation of motion that governs elastic waves in solids is written as (Graff, 1991):

$$\mathbf{M}\,\ddot{\mathbf{u}}(t) \;+\; \mathbf{K}\,\mathbf{u}(t) \;=\; \mathbf{F}(t), \tag{1}$$

where $\mathbf{M}$ and $\mathbf{K}$ are the mass and stiffness matrices, $\mathbf{u}(t)$ is the nodal displacement vector, and $\mathbf{F}(t)$ represents the external forces.

Elastic wave propagation across fractures is modeled based on the displacement discontinuity method (Pyrak-Nolte et al., 1990), representing each fracture as a zero-thickness internal interface with a non-welded contact. In this formulation, stress is continuous across the fracture, but displacement is discontinuous:

$$\sigma_n^+ \;=\; \sigma_n^-, \quad \sigma_s^+ \;=\; \sigma_s^-, \tag{2a}$$

$$u_n^+ - u_n^- \;=\; \frac{\sigma_n}{\kappa_n}, \quad u_s^+ - u_s^- \;=\; \frac{\sigma_s}{\kappa_s}, \tag{2b}$$

where σ, u, and κ denote stress, displacement, and specific stiffness, with subscripts n and s indicating normal and shear components, and superscripts $+/-$ referring to the two faces of the fracture.

To mimic an unbounded medium and absorb outgoing waves, we adopt a stiffness reduction method in which absorbing layers with thickness $1.5\,\lambda$ are appended around the computational domain (Lei & Sornette, 2021; Pettit et al., 2014), where λ is the central incident wavelength. Within these layers, the equation of motion is given by:

$$\mathbf{M}\,\ddot{\mathbf{u}}(t) \;+\; \mathbf{C}^*\,\dot{\mathbf{u}}(t) \;+\; \mathbf{K}^*\,\mathbf{u}(t) \;=\; \mathbf{F}(t), \tag{3}$$

with the effective damping and stiffness matrices defined by:

$$\mathbf{C}^* = \eta(\chi)\,\mathbf{M}, \quad \mathbf{K}^* = \zeta(\chi)\,\mathbf{K}, \tag{4}$$

where

$$\eta(\chi) = \omega\Big(\frac{\chi}{1.5\,\lambda}\Big)^3, \quad \alpha(\chi) = \alpha_{\max}\Big(\frac{\chi}{1.5\,\lambda}\Big)^3, \quad \alpha_{\max} = -\frac{\ln(\varepsilon)}{1.5\,\lambda\,k}, \quad \zeta(\chi) = \exp\big[-\alpha(\chi)\,k\,\chi\big]. \tag{5}$$

Here, $\mathbf{C}^*$ and $\mathbf{K}^*$ denote the spatially varying damping and stiffness in the absorbing layer. The scalar χ measures the distance into the absorbing layer from the boundary of the physical domain. The parameters ω and k are the angular frequency and wavenumber, respectively; $\varepsilon \ll 1$ is the prescribed attenuation threshold that controls the maximum decay at the outer edge of the absorbing layer. The function $\alpha(\chi)$ governs the cubic ramp of attenuation, with peak value $\alpha_{\max}$ chosen so that $\zeta(\chi = 1.5\,\lambda) = \varepsilon$.

2.2 Numerical Experiment Design

Synthetic fracture networks are generated inside a square domain of side length L. Each fracture is represented by a line segment whose length l is sampled from a truncated power-law distribution (Bonnet et al., 2001; Bour & Davy, 1997; Davy et al., 2010; Lei & Gao, 2018; Lei et al., 2015):

$$n(l) = \gamma\, l^{-a}, \quad l \in [\,l_{\min}, l_{\max}\,], \tag{6}$$

where $l_{\min} = L/100$ and $l_{\max} = 100\,L$ are the minimum and maximum fracture lengths, a is the power-law exponent, and γ is a normalization constant. Fracture centers are placed randomly in the domain and their orientations are drawn from a uniform distribution in $[0, 2\pi]$. To characterize each network, we compute the fracture density d and the percolation parameter p as (Darcel et al., 2003)

$$d = \frac{1}{L^2}\int_{l_{\min}}^{l_{\max}} n(l)\,l\,\mathrm{d}l, \tag{7}$$

$$p = \frac{1}{L^2}\int_{l_{\min}}^{l_{\max}} n(l)\,l^2\,\mathrm{d}l, \tag{8}$$

where p governs the fracture network connectivity, i.e., fracture networks are statistically connected if p exceeds the percolation threshold $p_c \approx 5.8$ (Bour & Davy, 1997). We explore four power-law exponents and four fracture density levels:

$$a \in \{1.5,\ 2.0,\ 2.5,\ 3.0\}, \qquad d \in \big\{12.5/L,\ 25.0/L,\ 37.5/L,\ 50.0/L\big\}.$$

For each (a, d) pair, we generate 10 independent random realizations, yielding a total of 160 synthetic networks. The percolation parameter p is computed for each realization (Figure 1). The connectivity parameter p is statistically related to both a and d, but is not uniquely determined by them due to realization-dependent variability.

Periodic boundary conditions are applied to the top and bottom of each fracture network model, while absorbing layers are imposed on the left and right sides (Figure 2). A five-cycle, Hann-windowed tone burst is applied along a source line at the left side of the domain to excite an incident plane P-wave with wavelength $\lambda = L/10$. A dense receiver array of 21×21 points is distributed across the domain. This array is used both to monitor wavefield evolution and to support the attenuation analysis underlying the estimation of Q^{-1}, based on the spatial decay of spectral amplitudes with source-to-receiver distance. The receiver layout is therefore adopted as a controlled numerical sampling design under well-resolved conditions, rather than as a representation of a typical field acquisition geometry. We set the domain size $L = 100$ m, rock density $\rho = 2650$ kg/m^3, and P- and S-wave velocities $V_p = 3685.8$ m/s and $V_s = 2128.0$ m/s. We explore fracture specific stiffness in the range $\kappa \in [0.226, 226]$ GPa/m,

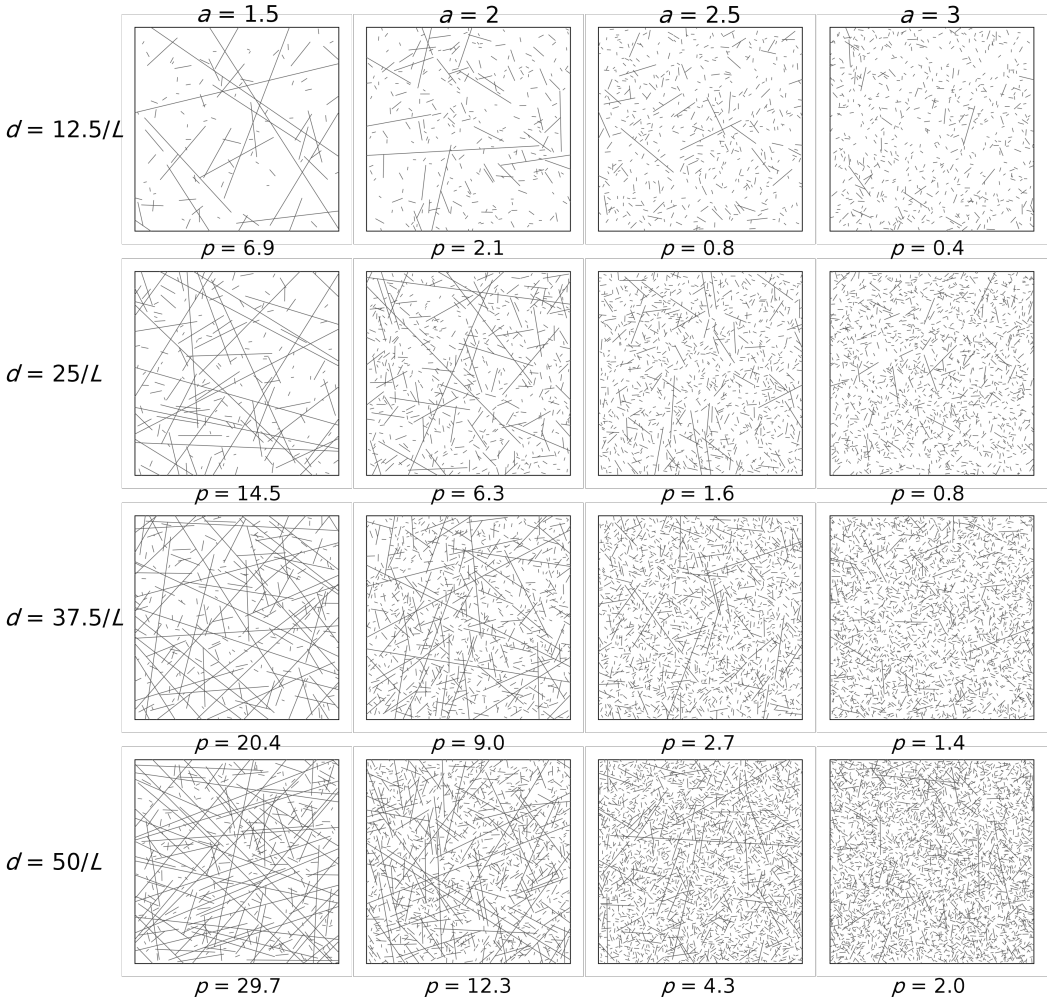

Figure 1. Representative fracture network realizations for combinations of length exponent a and fracture density d. The percolation parameter p is also indicated for each network.

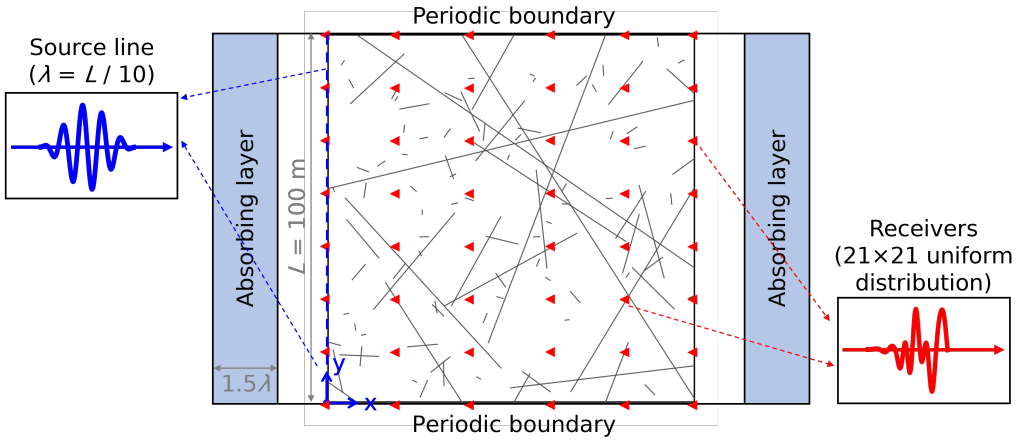

Figure 2. Numerical experiment setup: a square fracture network domain with periodic boundaries on the top and bottom, absorbing layers on the left and right, and a source line at the left side exciting an incident P-wave.

corresponding to 16 logarithmically spaced values of the dimensionless fracture stiffness $\tilde{\kappa} = \kappa/(\omega Z_p)$ within the interval [0.01, 10] (Lei & Sornette, 2021; Pyrak-Nolte et al., 1990), where $Z_p = \rho V_p$ is the P-wave impedance and ω is the angular frequency.

The domain is discretized using an unstructured triangular finite element mesh with an average element size of $\lambda/15$. At fracture intersections, the network is represented by connected internal boundary segments sharing common nodes, without assigning a separate effective stiffness to the intersections themselves. Each segment follows the stress-displacement relation in its own local normal–tangential coordinate system. An explicit time-integration scheme is used with a time step chosen to give a Courant-Friedrichs-Lewy number of 0.2 (Lei & Sornette, 2021). Combining the 160 synthetic fracture network realizations with 16 dimensionless fracture stiffness values yields $160 \times 16 = 2560$ forward simulations. All simulation results are reported in non-dimensional form throughout the paper.

We compute the inverse quality factor from the forward simulations using the spectral ratio method (Aki & Richards, 2002; Lei, 2022; Lei & Sornette, 2022):

$$Q^{-1} = -\frac{2\,V}{\omega\,x}\,\ln\!\Big(\frac{A}{A_0}\Big), \tag{9}$$

where V is the mean phase velocity of the P wave, x is the source-to-receiver distance, and A_0 and A are the spectral amplitudes of the source and received waves, respectively. The source and receiver records are transformed to the frequency domain using FFT over the full recorded time series, and the spectral amplitude at the incident frequency is extracted. For receivers at the same source-to-receiver distance, the logarithmic spectral amplitudes are averaged to obtain a mean amplitude A. The quantity $\ln(A/A_0)$ is then plotted against source-to-receiver distance, and a straight line is fitted to determine Q^{-1} (Frankel & Clayton, 1986). The arrival time is used only to estimate the mean propagation velocity V. In this study, Q^{-1} is used as an effective attenuation indicator at the incident frequency. An illustrative example of this calculation procedure is provided in the Supporting Information (Figure S1), following the same spectral ratio approach as adopted in Lei & Sornette (2021). In the present elastic-scattering framework, Q^{-1} reflects scattering-related attenuation and complements E, which summarizes the overall transmitted energy. We also monitor the normalized energy flux:

$$E \;=\; \frac{\displaystyle\sum_{j=1}^{N_r}\int_0^T \|\mathbf{u}_j(t)\|^2\,\mathrm{d}t}{\displaystyle\sum_{j=1}^{N_r}\int_0^T \|\mathbf{u}_{0,j}(t)\|^2\,\mathrm{d}t}\,, \tag{10}$$

where $N_r = 21$ is the number of receivers placed at the right boundary of the domain, T is the record duration, $\mathbf{u}_j(t)$ is the displacement vector at receiver j in the given fracture network realization, and $\mathbf{u}_{0,j}(t)$ is the displacement in a reference case without fractures. These two metrics, Q^{-1} and E, complementarily reflect the wave transport behavior. Specifically, the inverse quality factor Q^{-1} emphasizes early-time amplitude decay of the coherent, propagating wavefield, whereas the normalized energy flux E accounts for the total transmitted energy over time, including late-time scattered and diffusive components. By jointly analyzing Q^{-1} and E, we obtain a more complete view of the temporal evolution of wave energy, from early-stage propagation to late-stage diffusive transport.

2.3 Distance-based Generalized Sensitivity Analysis (DGSA)

We employ DGSA to assess the influence of the input parameters $(\tilde{\kappa}, a, d, p)$ on the two wave-transport metrics (Q^{-1}, E). First, all 2560 simulation outputs are grouped into $C = 5$ clusters in the (Q^{-1}, E) plane using K-medoids with Euclidean distance, because this choice provides the clearest correspondence with the five physically interpretable response regimes while preserving stable DGSA sensitivity patterns for nearby values of C. For each

input parameter θ_i, we compute the L_1 distance between its overall empirical cumulative distribution function (CDF) and the CDF conditioned on membership in each cluster. To make these distances comparable across clusters, each is normalized by the 0.95-quantile of that cluster's own within-sample distances. We then average the normalized distances over all clusters to obtain a sensitivity index $S(\theta_i)$; parameters with $S > 1$ are deemed sensitive (Chen et al., 2025; Scheidt et al., 2018; Tas, Hartog, et al., 2025).

DGSA is suitable for our study because it (i) works directly on the joint (Q^{-1}, E) outputs without prior dimensionality reduction, (ii) naturally handles mixed-type inputs (continuous and discrete parameters) in a single framework, and (iii) requires far fewer model runs than variance-based methods such as Sobol indices (Park et al., 2016). In addition, the cluster-based formulation yields a regime-focused view of how each parameter shapes wave transport behavior (L. Zhang, Dieudonné, et al., 2025; L. Zhang, Mi, et al., 2025). See Appendix A for mathematical details of the DGSA framework.

2.4 Bayesian Inversion Framework

We denote the vector of unknown fracture network parameters as

$$\theta = (a, d, p),$$

where a is chosen from the discrete set $\{1.5, 2.0, 2.5, 3.0\}$, d from $\{12.5/L, 25.0/L, 37.5/L, 50.0/L\}$, and p is the percolation parameter. The observed data consist of the two wave transport metrics

$$y = \left(Q_{\text{obs}}^{-1}, E_{\text{obs}}\right),$$

measured at a known dimensionless stiffness $\tilde{\kappa}_{\text{obs}}$. The 2560 forward simulations are split into 60% for surrogate training, 20% for noise estimation used in the likelihood model, and 20% for independent validation. This split separates surrogate fitting, calibration of the residual-error model, and final out-of-sample performance assessment. Estimating residual statistics on the training data would lead to overly optimistic error characterization, while the 60% training subset remains sufficient for accurate surrogate fitting.

By Bayes' theorem (Hermans et al., 2019, 2016; L. Zhang et al., 2026), the posterior distribution of θ given y and $\tilde{\kappa}_{\text{obs}}$ is

$$p\left(a, d, p \mid y, \tilde{\kappa}_{\text{obs}}\right) \;\propto\; p(a)\, p(d)\, p\left(p \mid a, d\right) p\left(y \mid a, d, p, \tilde{\kappa}_{\text{obs}}\right). \tag{11}$$

We assign uniform priors over the four discrete values of a and d:

$$p\left(a = a_i\right) \;=\; \frac{1}{4}, \quad i = 1, \ldots, 4, \qquad p\left(d = d_j\right) \;=\; \frac{1}{4}, \quad j = 1, \ldots, 4,$$

and a conditional Gaussian prior for p at each (a, d) pair:

$$p\left(p \mid a, d\right) = \mathcal{N}\left(\mu_{ad},\, \sigma_{ad}^2\right),$$

where μ_{ad} and σ_{ad} are the sample mean and standard deviation computed from the 10 realizations for each (a, d) pair.

To replace the computationally expensive forward model $(a, d, p, \tilde{\kappa}) \mapsto (Q^{-1}, E)$, we train a random forest surrogate on the training set,

$$(\widehat{Q}^{-1},\, \widehat{E}) = f(a, d, p, \tilde{\kappa}). \tag{12}$$

All inputs $X = (a, d, p, \tilde{\kappa})$ and outputs $Y = (Q^{-1}, E)$ are standardized as

$$X_{\text{std}} = \frac{X - \bar{X}}{s_X}, \quad Y_{\text{std}} = \frac{Y - \bar{Y}}{s_Y},$$

using the empirical means $\bar{X}, \bar{Y}$ and standard deviations s_X, s_Y of the training data.

Residuals $\left(Q_{\text{obs}}^{-1} - \widehat{Q}^{-1},\ E_{\text{obs}} - \widehat{E}\right)$ are modeled as a bivariate normal with zero mean, marginal standard deviations σ_Q, σ_E, and correlation ρ. Here, ρ is the Pearson correlation coefficient between the two residual components, estimated on the 20% subset reserved for noise estimation. Defining

$$z_Q = \frac{Q_{\text{obs}}^{-1} - \widehat{Q}^{-1}}{\sigma_Q}, \quad z_E = \frac{E_{\text{obs}} - \widehat{E}}{\sigma_E},$$

the likelihood is written as

$$p(Q_{\text{obs}}^{-1}, E_{\text{obs}} \mid \theta, \tilde{\kappa}_{\text{obs}}) = \frac{1}{2\pi\sqrt{1-\rho^2}} \exp\Big[-\tfrac{1}{2(1-\rho^2)}\left(z_Q^2 - 2\rho\, z_Q z_E + z_E^2\right)\Big]. \tag{13}$$

We draw $N_{\text{samp}} = 3000$ posterior samples (after discarding a burn-in of $N_{\text{burn}} = 500$) using the Metropolis-Hastings algorithm with switch-move probability $p_{\text{switch}} = 0.3$ and perturbation scale $\gamma = 0.3$. At each step, (i) with probability p_{switch}, redraw (a', d') uniformly and sample $p' \sim \mathcal{N}(\mu_{a'd'}, \sigma^2_{a'd'})$; (ii) otherwise, keep (a, d) fixed and set $p' = p + \varepsilon$, $\varepsilon \sim \mathcal{N}(0, \gamma\, \sigma_{ad})$. The acceptance probability for $\theta \to \theta'$ is:

$$\alpha = \min\left\{1,\ \frac{p(\theta')\, p(Q_{\text{obs}}^{-1}, E_{\text{obs}} \mid \theta', \tilde{\kappa}_{\text{obs}})}{p(\theta)\, p(Q_{\text{obs}}^{-1}, E_{\text{obs}} \mid \theta, \tilde{\kappa}_{\text{obs}})}\right\}. \tag{14}$$

3 Results

3.1 Forward Simulation

Figure 3 shows the forward simulations by plotting the normalized displacement component u_x along the x direction at two dimensionless times $\tilde{t} = tV_p/L = 1$ and 2 for four values of the dimensionless fracture stiffness $\tilde{\kappa} = 0.01$, 0.1, 1, 10. The corresponding seismograms recorded by the receivers placed at the right boundary of the domain are also shown. Panels (a)-(d) correspond to the fracture network parameter combinations

$$(a, d) = (1.5,\ 12.5/L),\ (3,\ 12.5/L),\ (1.5,\ 50/L),\ (3,\ 50/L),$$

respectively, and illustrate how fracture connectivity influences the wavefield patterns and recorded seismograms across different values of $\tilde{\kappa}$.

As shown in Figure 3, for $\tilde{\kappa} = 10$, the wavefield exhibits a smooth, nearly planar wavefront and the incident waveform is well preserved in the seismograms. For $\tilde{\kappa} = 1$, multiple scattering generates pronounced coda waves, visible in both the displacement field and the seismograms. When $\tilde{\kappa}$ is reduced to 0.1, the waves become strongly scattered and diffusive, producing long-lasting coda trains. For $\tilde{\kappa} = 0.01$, waves are effectively trapped by the fracture network, especially for small a and large d. These examples illustrate how fracture stiffness and network geometry jointly influence wavefield behavior. As $\tilde{\kappa}$ decreases, scattering becomes stronger, coda waves become more pronounced, and coherent transmission is progressively reduced. These effects are more evident in better connected networks associated with smaller a and larger d.

The wavefield responses considered here are grouped into five transport regimes: propagation, superdiffusion, normal diffusion, subdiffusion, and localization (Bouchaud & Georges, 1990; Lei & Sornette, 2021, 2022). The propagation regime is characterized by coherent transmission with limited scattering and clear first arrivals; the superdiffusion and normal diffusion regimes correspond to progressively stronger multiple scattering and coda development while wave energy still spreads through the network; the subdiffusion regime reflects slowed spreading with partial trapping; and the localization regime corresponds to the strongest confinement of wave energy that is trapped in the system.

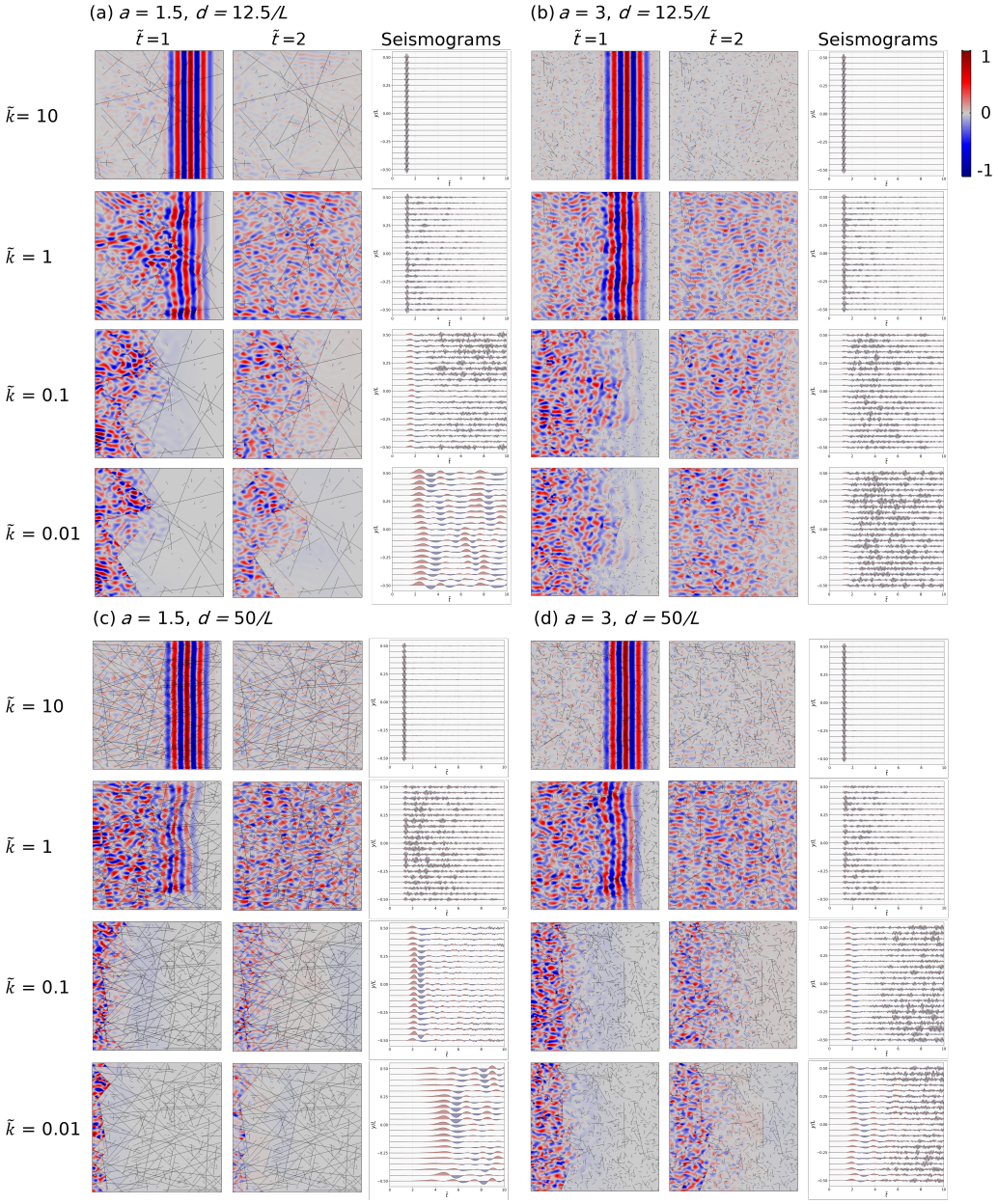

Figure 3. Normalized displacement u_x at dimensionless times $\tilde{t} = t/(L/V_p) = 1, 2$ (left columns) and corresponding seismograms (right column) for dimensionless fracture stiffness $\tilde{\kappa} = 0.01, 0.1, 1, 10$. Panels (a)-(d) correspond to different pairs of power-law exponent and fracture density, $(a, d) = (1.5, 12.5/L), (3, 12.5/L), (1.5, 50/L), (3, 50/L)$.

3.2 Sensitivity Analysis

We now perform a quantitative analysis of wavefield behavior by extracting the two scalar metrics, the inverse quality factor Q^{-1} and the normalized energy flux E, for all 2560 simulations and assessing their sensitivity to the four model parameters a, d, p, and $\tilde{\kappa}$.

Figure 4a shows a strong negative correlation between Q^{-1} and E ($\rho \approx -0.92$). K-medoids clustering in the $\left(E, \log_{10} Q^{-1}\right)$ space partitions the simulations into five groups that correspond closely to the five transport regimes defined in Section 3.1, namely propagation, superdiffusion, normal diffusion, subdiffusion, and localization. The resulting DGSA sensitivity indices (Figure 4b) quantify the influence of each parameter:

$$S(\tilde{\kappa}) = 8, \quad S(d) = 2.4, \quad S(p) = 1.7, \quad S(a) = 1.2,$$

all exceeding the threshold $S = 1$. The dimensionless fracture stiffness $\tilde{\kappa}$ exerts the strongest control on (Q^{-1}, E), followed by fracture density d, percolation parameter p, and power-law exponent a.

The cluster-conditional empirical cumulative distribution functions (CDFs) in Figures 4c-f clarify how the parameters vary across the five transport regimes. The strongest separation is observed for $\tilde{\kappa}$. Nearly all realizations in the propagation, superdiffusion, and normal diffusion clusters have $\tilde{\kappa} > 1$, whereas these regimes disappear once $\tilde{\kappa} \lesssim 0.25$. At lower $\tilde{\kappa}$, the realizations fall almost exclusively into the subdiffusion and localization clusters, confirming that fracture stiffness is the primary control on the overall transport regime.

The network parameters d, p, and a show weaker but still systematic trends. Higher fracture density, higher percolation parameter, and smaller power-law exponent shift realizations toward subdiffusion and localization, consistent with stronger connectivity and scattering. Their role becomes clearest when comparing subdiffusion with localization. Both clusters occur at similarly small $\tilde{\kappa}$, but the subdiffusion cases are associated with less connected networks, with lower d, lower p, and larger a, indicating predominantly shorter fractures. This contrast shows that, once fractures are sufficiently compliant, network connectivity determines whether transport remains subdiffusive or progresses to localization.

Building on these DGSA results, with $\tilde{\kappa}$ identified as the dominant control on (Q^{-1}, E), we next examine how the relative importance of the input parameters evolves with fracture stiffness. We partition the 16 logarithmically spaced values of $\tilde{\kappa}$ into 14 overlapping windows, each containing three consecutive values, and recompute $S(\tilde{\kappa})$, $S(d)$, $S(p)$, and $S(a)$ within each window. Figure 5 shows these sensitivity indices as functions of the central $\tilde{\kappa}$ value of the corresponding window.

For $\tilde{\kappa} > 1$, the index $S(\tilde{\kappa})$ remains above 4 and varies little across windows, while the indices for the fracture network parameters are nearly constant: $S(d)$ fluctuates around 2, $S(p)$ stays just above 1, and $S(a)$ remains modest. In this regime, the wavefield is dominated by propagation and superdiffusion, where individual fractures contribute to attenuation and transmission with limited collective interaction.

As $\tilde{\kappa}$ decreases into the intermediate-stiffness band ($0.25 \lesssim \tilde{\kappa} \leq 1$), $S(\tilde{\kappa})$ gradually declines and the sensitivities of d, p, and a begin to rise. Here, the effect of individual fracture stiffness is still slightly stronger, but interactions between fractures have started to exert a more pronounced influence on wavefield evolution. The decline in $S(\tilde{\kappa})$ together with the increase in $S(d)$ signals the growing role of multiple scattering and collective interaction.

Between $\tilde{\kappa} \approx 0.1$ and 0.25, the sensitivity to stiffness drops sharply, falling below the threshold $S = 1$ by $\tilde{\kappa} = 0.1$, while the fracture network parameters increase steeply, particularly the density, which becomes the most influential. In this range, the wavefield enters the subdiffusion and localization regimes: waves must meander through gaps in between neighboring fractures within the fracture network, so network pattern and connectivity have more impact on transmission and attenuation than the stiffness of individual fractures.

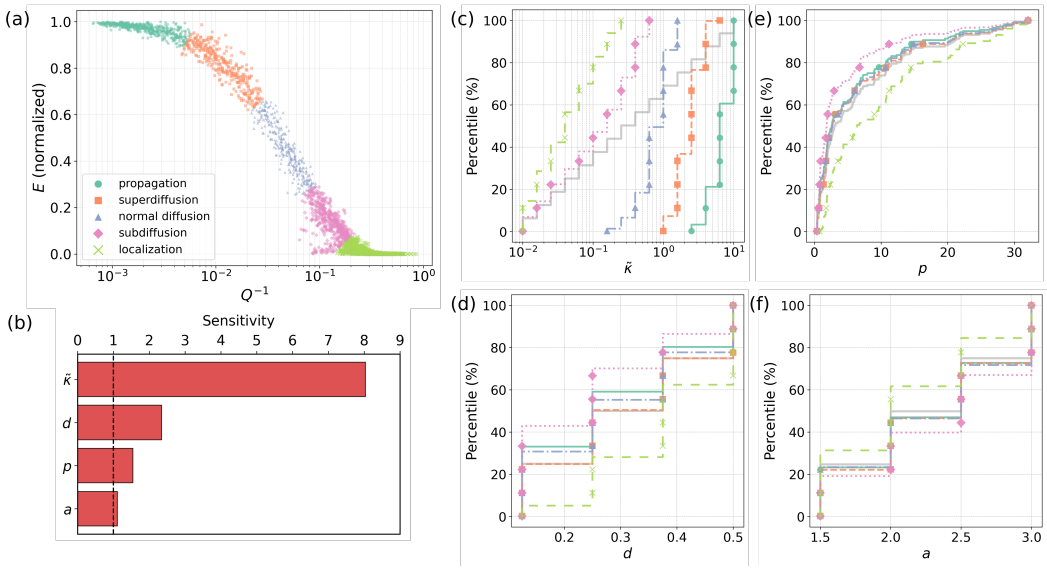

Figure 4. DGSA applied to the wave transport metrics (Q^{-1}, E) of the 2560 realizations. **(a)** Scatter of $\log_{10} Q^{-1}$ and E, grouped by K-medoids transport regimes: propagation, superdiffusion, normal diffusion, subdiffusion, and localization. Regimes are distinguished by both color and marker type. **(b)** Sensitivity indices $S(\tilde{\kappa}) = 8$, $S(d) = 2.4$, $S(p) = 1.7$, and $S(a) = 1.2$; the dashed line marks $S = 1$. **(c-f)** Regime-conditional empirical CDFs for $\tilde{\kappa}$, p, d, and a, respectively. Regimes are distinguished by consistent colors, marker types, and line styles across panels.

For $\tilde{\kappa} < 0.1$, $S(\tilde{\kappa})$ collapses toward zero, indicating that further reductions in the dimensionless stiffness no longer affect (Q^{-1}, E). In contrast, $S(d)$, $S(p)$, and $S(a)$ stabilize in the range 3-4, reflecting a regime in which wave transport is governed almost entirely by fracture network properties. In this limiting scenario, multiple scattering and wave interference within the network dominate the overall wavefield behavior.

3.3 Surrogate Construction, Validation, and Bayesian Inversion

The DGSA results show that the input parameters a, d, p, and $\tilde{\kappa}$ all have a significant impact on the two wave transport metrics (Q^{-1}, E). This indicates that information on these parameters is present in the observations. To make inversion computationally feasible, and to reflect typical seismic settings in which the source frequency (and hence $\tilde{\kappa}_{\text{obs}}$) is prescribed, we construct a forward surrogate model $f\colon (a, d, p, \tilde{\kappa}) \mapsto (\widehat{Q}^{-1}, \widehat{E})$ and embed it in a Bayesian sampling scheme to estimate the joint posterior distribution of (a, d, p) given observed $(Q^{-1}_{\text{obs}}, E_{\text{obs}})$ at known $\tilde{\kappa}_{\text{obs}}$.

We train the random forest surrogate using 60% of the 2560 forward simulations and reserve two independent 20% subsets for noise estimation and validation, respectively. On the independent validation set, the surrogate achieves prediction coefficients of determination $R^2(Q^{-1}) = 0.995$ and $R^2(E) = 0.996$ (Figure 6). The prediction residuals

$$\varepsilon_Q = Q^{-1}_{\text{true}} - \widehat{Q}^{-1}, \quad \varepsilon_E = E_{\text{true}} - \widehat{E}$$

are approximately zero-mean Gaussian, from which we estimate marginal standard deviations σ_Q, σ_E and correlation ρ. These statistics define the bivariate normal likelihood described in Section 2.4.

We perform posterior sampling with the Metropolis-Hastings algorithm, using four parallel chains on 20 randomly selected validation cases. Gelman-Rubin diagnostics yield $\hat{R}$

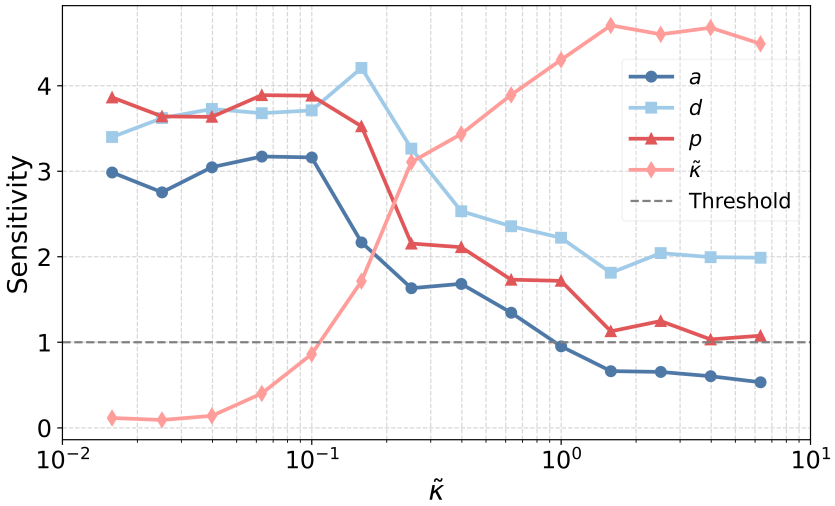

Figure 5. Sensitivity indices $S(\tilde{\kappa})$, $S(d)$, $S(p)$, and $S(a)$ as functions of the central value of $\tilde{\kappa}$ in each sliding window. The dashed line indicates the threshold $S = 1$.

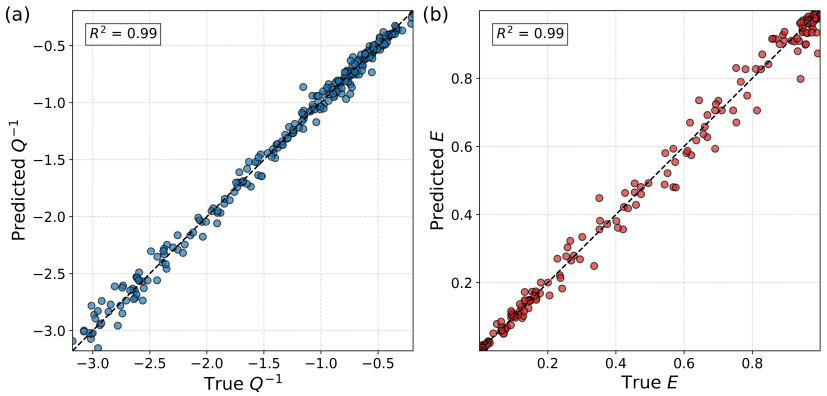

Figure 6. Surrogate predictions vs. true values on the test set regarding the two wave transport metrics: (a) Q^{-1}, with the coefficient of determination $R^2 = 0.995$, and (b) E, with $R^2 = 0.996$.

statistics below 1.05 for a, d, and p (with a median of approximately 1.01 and a worst case below 1.03), indicating a good mixing of all chains (Figure 7) (Gelman & Rubin, 1992).

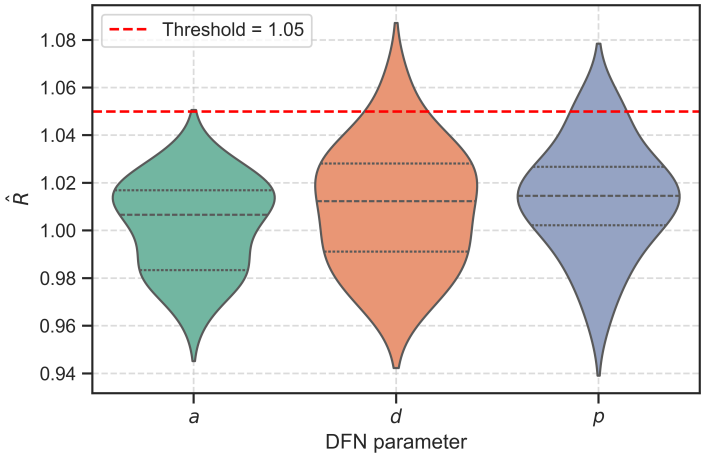

Figure 7. Gelman-Rubin $\hat{R}$ statistics across 20 validation draws (four chains each) for the three inferred parameters a, d, and p. The red dashed line marks $\hat{R} = 1.05$.

To illustrate parameter recoverability in different wavefield regimes, we select one representative realization from each of the five clusters (propagation, superdiffusion, normal diffusion, subdiffusion, and localization) and compare the prior and posterior marginals for the discrete parameters a and d, together with the conditional prior and posterior density of p (Figure 8). In each row, dashed vertical lines mark the true values, stars indicate the posterior mode (MAP), and, for the continuous parameter p, the shaded band denotes the 95% credible interval. Three characteristic inversion behaviors emerge. In the first, the posteriors for a and d collapse tightly around the true values, and the conditional posterior for p peaks at the true percolation. In the second, the marginals for a and d exhibit multiple comparably weighted modes, which induces a multi-peaked posterior for p that nonetheless contains the correct value within its high-probability regions. Finally, we observe cases in which the true a or d lies within one of the two highest-probability modes rather than at the global maximum; in these cases, a maximum a posteriori (MAP) estimate would not select the true value, but the posterior concentration remains much stronger than in the prior, indicating substantial uncertainty reduction.

To assess inversion performance across the entire validation set, we ran Metropolis-Hastings on all held-out samples, recorded the most probable estimates of a and d for each case, and then grouped these results by $\tilde{\kappa}$. Figure 9 shows the mean probability that the inferred a or d equals its true value in each group. These recovery rates almost always exceed the uniform prior level of 0.25, showing that the random forest surrogate combined with the Bayesian likelihood does extract information on both parameters from (Q^{-1}, E). Moreover, fracture density d is consistently better identified than the power-law exponent a, in line with the global sensitivity result $S(d) > S(a)$ for all $\tilde{\kappa}$.

In the high fracture stiffness range ($\tilde{\kappa} \gtrsim 0.25$), inversion performance improves markedly over the prior. In several stiffness windows, the mean recovery probability for the exponent a exceeds 40%, and for the density d exceeds about 60%, with the strongest performance near $\tilde{\kappa} \approx 1$. In this band, the sliding-window DGSA indicates that individual fracture stiffness remains the dominant control, or acts together with the network properties, with $S(\tilde{\kappa}) \gg 1$ and $S(d)$, $S(p)$, and $S(a)$ all showing significant sensitivity. Treating the observed

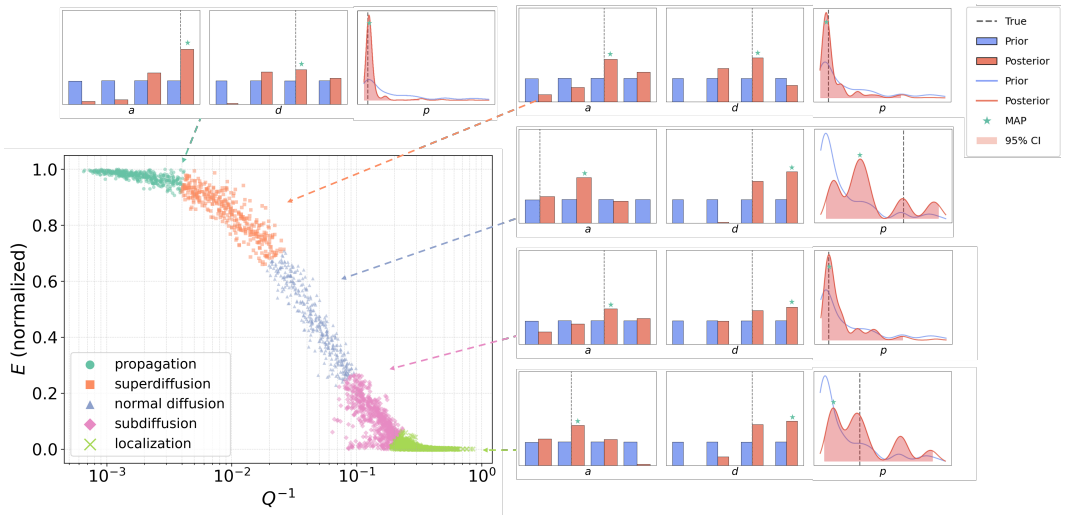

Figure 8. Prior and posterior marginals for a (left), d (center), and p (right) for one representative example from each DGSA transport regime. True values are indicated by dashed vertical lines. For the discrete parameters a and d, stars mark the posterior mode (MAP). For the percolation parameter p, the posterior MAP and the 95% credible interval are shown. The marginal posterior of p may be multimodal because p is inferred jointly with the discrete parameters a and d. Colors and dashed connectors identify the corresponding regime in the (Q^{-1}, E) space.

dimensionless stiffness $\tilde{\kappa}_{\text{obs}}$ as known therefore sharply reduces the posterior uncertainty of both a and d relative to their uniform priors.

For low fracture stiffness range $\tilde{\kappa} \lesssim 0.25$, the sensitivity index $S(\tilde{\kappa})$ collapses, dropping below 1 by $\tilde{\kappa} = 0.1$ and continuing to decline at smaller $\tilde{\kappa}$. In this regime, fracture network properties dominate the wavefield, so conditioning on $\tilde{\kappa}_{\text{obs}}$ tends to amplify measurement noise and broaden the posterior. The mean recovery probability for the exponent a then falls back to only slightly above the uniform prior level, while that for the density d, although still higher than for a, decreases to about 45%, a clear decline compared with the high stiffness range.

These results show that the accuracy of fracture network parameter inversion, when conditioned on both the wave transport metrics (Q^{-1}, E) and the observed dimensionless stiffness $\tilde{\kappa}_{\text{obs}}$, depends strongly on which physical process dominates the wavefield. The best performance occurs around $\tilde{\kappa} \approx 1$, where individual-fracture stiffness is still the primary control even though fracture network effects begin to contribute. In this regime, $\tilde{\kappa}_{\text{obs}}$ acts as a highly informative constraint, yielding concentrated posteriors for both a and d, and DGSA confirms that both parameters are sensitive here. In contrast, in the low stiffness regime ($\tilde{\kappa} \lesssim 0.25$), the effect of fracture network properties prevails, sensitivity to $\tilde{\kappa}_{\text{obs}}$ collapses, and inversion accuracy declines. This highlights that aligning inversion constraints with parameters to which the observables are most sensitive improves recovery, whereas conditioning on weakly sensitive variables can introduce extra uncertainty and degrade performance.

Figure 10 further quantifies the inversion performance by plotting, for each $\tilde{\kappa}$ window, the probability that the true parameter lies among the two highest-probability posterior values for a (blue circles) and d (red squares), with the uniform prior benchmarked at 0.5. Consistent with the results above, the top-two recovery rate for a rises from about 0.55 at $\tilde{\kappa} = 0.1$ to 0.8 at $\tilde{\kappa} \approx 1$, then declines back toward 0.5 in the low stiffness regime. In

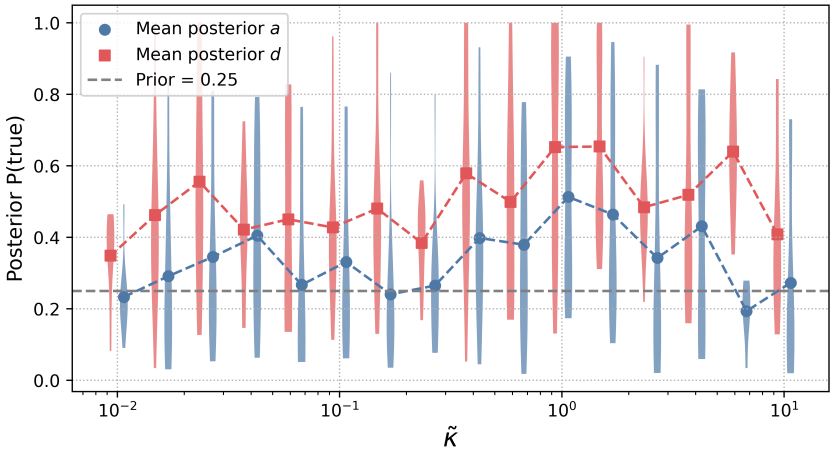

Figure 9. Mean posterior recovery probabilities for a (blue circles) and d (red squares) across all validation cases, plotted against $\tilde{\kappa}$. The dashed line indicates the prior level of 0.25.

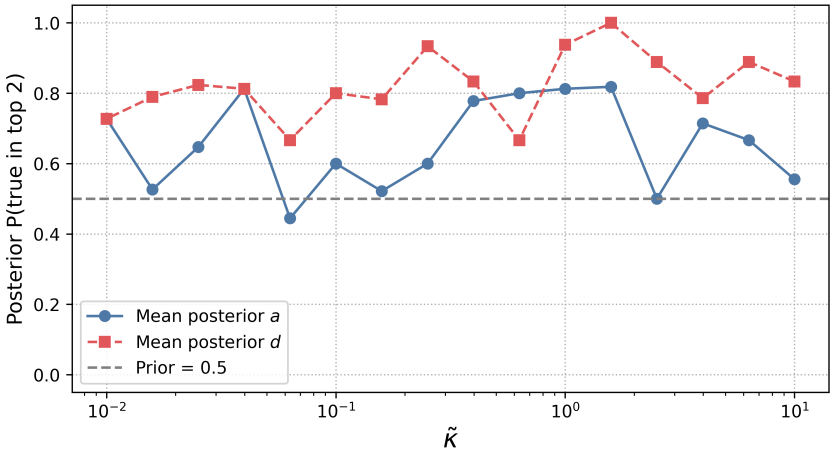

Figure 10. Probability that the true parameter value lies among the two highest-probability posterior values for a (blue circles) and d (red squares) across all validation cases, plotted against $\tilde{\kappa}$. The dashed line indicates the prior level of 0.5.

contrast, d maintains a top-two probability above 0.8 across all windows, peaks at 1.0 near $\tilde{\kappa} \approx 1$, and then stabilizes around 0.8 at the smallest $\tilde{\kappa}$ values. These top-two recovery probabilities exceed the prior baseline in every stiffness band and mirror the trends seen in the single-value recovery rates and in the sensitivity analysis: inversion is most reliable when fracture stiffness dominates the response ($\tilde{\kappa} \approx 1$) and gradually degrades as network-scale effects take over at smaller $\tilde{\kappa}$.

To confirm that the inferred MAP parameters are consistent with the observed wave features under our surrogate-based likelihood, we perform a posterior predictive check. For each validation case, we evaluate the random forest surrogate

$$(\widetilde{Q}^{-1},\, \widetilde{E}) = f\big(\hat{a}, \hat{d}, \hat{p},\, \tilde{\kappa}_{\mathrm{obs}}\big)$$

at the MAP parameters $\hat{\theta} = (\hat{a}, \hat{d}, \hat{p})$. Figure 11 compares these predictions to the true values of Q^{-1} and E across all validation examples and yields $R^2 \approx 0.99$ in both panels. This

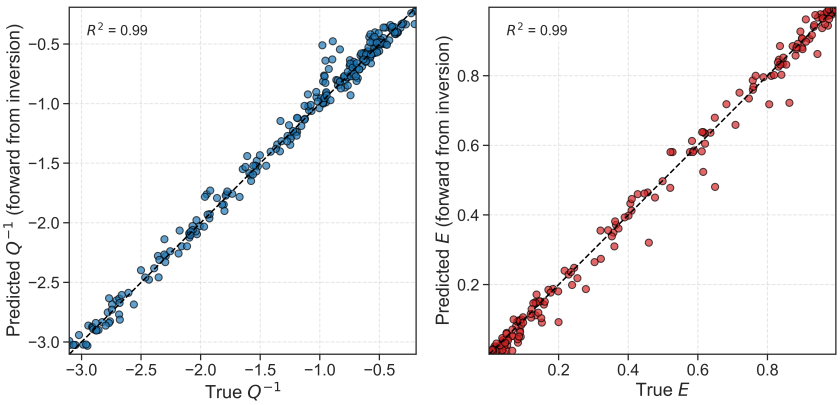

Figure 11. Posterior predictive check: surrogate outputs $\widetilde{Q}^{-1}$ and $\widetilde{E}$ at the MAP fracture network parameters versus the true observed values. Both panels achieve $R^2 \approx 0.99$.

close agreement reflects the fact that the likelihood explicitly enforces consistency between surrogate outputs and observed features, thereby supporting the internal consistency of the inversion framework.

4 Discussion

4.1 Sensitivity, Identifiability, and Uncertainty Reduction

Sensitivity analysis quantifies how variations in model inputs θ_i affect model outputs y, providing an initial step toward understanding which parameters drive system behavior. DGSA extends this approach by partitioning output realizations into clusters and computing the L_1 distance between the unconditional and cluster-conditional empirical cumulative distribution functions of each parameter. The resulting global index $S(\theta_i)$ measures the information contribution of θ_i to the model response (Hermans et al., 2018; Scheidt et al., 2018). In inverse uncertainty quantification, identifiability denotes the extent to which observational data can constrain a parameter's true value. Highly identifiable parameters exhibit narrow, unimodal posteriors, whereas non-identifiable parameters yield broad or multimodal distributions (Arendt, Apley, & Chen, 2012; Arendt, Apley, Chen, Lamb, & Gorsich, 2012). Since sensitivity gauges how strongly a parameter influences observables, it directly underpins identifiability: if $S(\theta_i) \gg 1$, the data contain enough information to concentrate the posterior of θ_i; conversely, if $S(\theta_i) \approx 0$, then θ_i remains essentially invisible to the data and its posterior remains close to the prior.

Empirical and theoretical studies have confirmed this link between sensitivity and posterior uncertainty. For instance, in complex water-quality models, Bayesian calibration has shown that parameters with low sensitivity retain nearly uniform posteriors despite extensive data, whereas high-sensitivity parameters converge sharply, illustrating the "high S-low variance" pattern (Jia et al., 2018). Similarly, calibration of nuclear reactor models using Sobol indices has demonstrated that only parameters with significant sensitivity can be statistically identified, while those with near-zero sensitivity yield flat posteriors regardless of the inference method (Wu et al., 2019). In our sensitivity study (Figure 5), the index $S(d)$ consistently exceeds $S(a)$ across all stiffness ranges; accordingly, the identifiability of the fracture density d in Figure 9 (as seen in its higher recovery rate and narrower credible intervals) is superior to that of the power-law exponent a.

Within our inversion framework, the distance-based analysis reveals three stiffness-dependent sensitivity regimes that directly predict identifiability and uncertainty. For the

high stiffness band with $\tilde{\kappa} \gtrsim 1$, the sensitivity index $S(\tilde{\kappa}) \approx 4.8$ far exceeds those of a, d, and p. Although this indicates that $\tilde{\kappa}$ dominates the wavefield evolution, because $\tilde{\kappa}$ is held fixed during inversion, nearly all of the data's information about stiffness is used to confirm the known value rather than to constrain network parameters. As a result, the fracture network parameters remain only moderately identifiable and their posteriors are broader than they would be if the data are primarily sensitive to a, d, or p.

In the intermediate stiffness band ($0.25 \lesssim \tilde{\kappa} \lesssim 1$), sensitivity shifts gradually from $\tilde{\kappa}$ to the network parameters: $S(d)$ and $S(p)$ increase while $S(\tilde{\kappa})$ declines. Here, inversion of (a, d, p) yields substantial posterior concentration for d and p, reflecting their growing influence on (Q^{-1}, E), whereas the exponent a remains less tightly constrained. For the low stiffness band with $\tilde{\kappa} \lesssim 0.25$, $S(\tilde{\kappa}) \approx 0$ indicates that stiffness no longer drives the seismic response, while network parameters dominate. Intuitively, this should improve identifiability of (a, d, p); in practice, however, conditioning on a non-informative $\tilde{\kappa}$ introduces additional uncertainty into the likelihood and broadens the posteriors. Reducing uncertainty and improving identifiability requires aligning data acquisition and inversion constraints with the sensitivity spectrum as revealed by our analysis. This entails conditioning only on informative variables and targeting the regimes where each parameter exerts maximal influence.

4.2 Inferring Fracture Stiffness

In the analysis above, we treated the dimensionless stiffness $\tilde{\kappa}$ as known and focused on inverting the fracture network parameters (a, d, p). DGSA, however, showed that $\tilde{\kappa}$ is the most influential parameter for the wave transport metrics (Q^{-1}, E), which naturally raises the question of how well fracture stiffness itself can be inferred from these observables when it is not prescribed.

To address this, we performed a complementary inversion experiment in which all four parameters $(a, d, p, \tilde{\kappa})$ are treated as unknown and inferred jointly from (Q^{-1}, E). We reuse the random forest surrogate $f(a, d, p, \tilde{\kappa})$ and the Gaussian likelihood described in Section 2.4, and assign a discrete uniform prior to $\tilde{\kappa}$ over the 16 simulated stiffness levels (prior probability $1/16$ for each level). For each validation case, we compute the posterior probability mass assigned to the true stiffness level and then average this quantity over all cases whose true $\tilde{\kappa}$ falls into the same stiffness bin.

Figure 12 summarizes the resulting recovery probabilities as a function of $\tilde{\kappa}$. For low stiffnesses ($\tilde{\kappa} \lesssim 0.1$), the mean posterior probability of the true stiffness is only slightly above the prior level, indicating that (Q^{-1}, E) contain limited information about $\tilde{\kappa}$ in this regime when the network parameters are also unknown. As $\tilde{\kappa}$ increases into the intermediate range ($\tilde{\kappa} \approx 0.3{-}1$), the posterior mass at the true stiffness rises to about 0.3-0.4, and for high stiffnesses ($\tilde{\kappa} \gtrsim 3$) it reaches 0.6-0.7, i.e., a clear improvement over the prior. Although individual realizations still exhibit variability, the overall trend is robust: stiffer fractures are systematically easier to recover from the wave transport metrics.

These results are consistent with the DGSA findings in Figure 5. In the propagation and superdiffusion regimes (large $\tilde{\kappa}$), where the response is highly sensitive to fracture stiffness, the seismogram features carry enough information to constrain $\tilde{\kappa}$ even when the network parameters (a, d, p) are inferred simultaneously. In contrast, in the subdiffusion and localization regimes (small $\tilde{\kappa}$), where the wavefield is controlled primarily by fracture network properties, the posterior probability of the true $\tilde{\kappa}$ remains close to the prior, reflecting poor identifiability of fracture stiffness. Together with the network parameter inversions, this stiffness-focused experiment shows that the framework naturally delineates complementary regimes in which individual fracture stiffness, fracture network geometry, or both can be stably inferred from simple wave transport metrics.

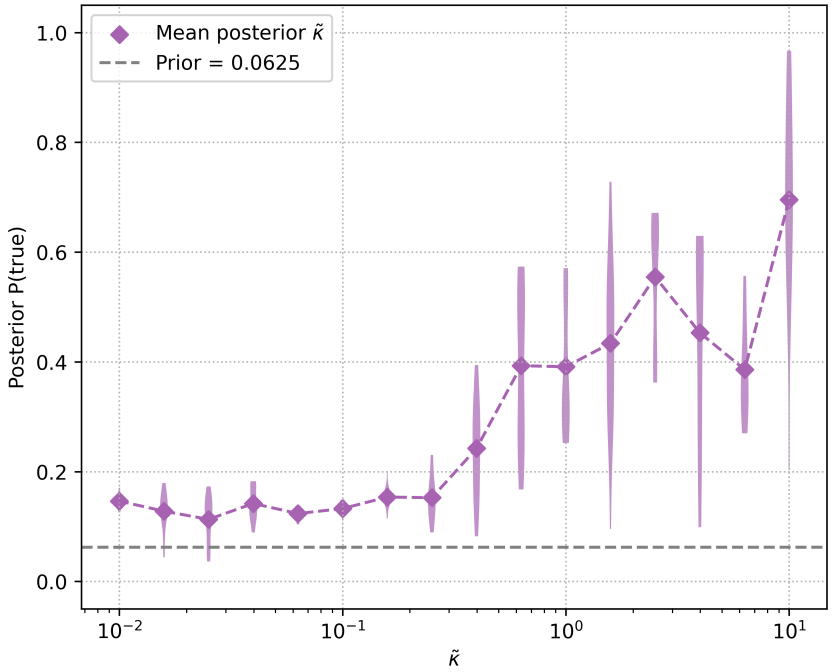

Figure 12. Mean posterior probability assigned to the true dimensionless stiffness $\tilde{\kappa}$ across all validation examples, binned by $\tilde{\kappa}$. Diamonds denote bin-averaged values and vertical violins show the distribution within each bin. The dashed line indicates the prior probability (1/16).

4.3 Information Limits in the Soft-Fracture Regime

The DGSA and inversion results together show that stiffness sensitivity collapses in the soft-fracture regime ($\tilde{\kappa} \lesssim 0.25$), where wave propagation is controlled mainly by fracture network properties rather than by individual-fracture stiffness. In this range, only (a, d, p) retain significant sensitivity, while $S(\tilde{\kappa})$ is close to zero.

This collapse has direct implications for inversion design. When $S(\tilde{\kappa}) \approx 0$, conditioning on $\tilde{\kappa}_{\text{obs}}$ is unlikely to add useful information about (a, d, p) and may instead introduce extra noise into the likelihood. To test this, we repeated the surrogate construction and Bayesian inversion for all validation cases with $\tilde{\kappa} \leq 0.1$, omitting $\tilde{\kappa}_{\text{obs}}$ altogether. Specifically, we trained a new random forest surrogate

$$f' \colon (a, d, p) \mapsto (Q^{-1}, E)$$

using the same 60/20/20 split of the forward simulations, and then ran Metropolis-Hastings on the held-out cases under the same likelihood formulation but without conditioning on $\tilde{\kappa}$. Despite the reduced input set, the surrogate maintains good predictive accuracy on the test set, with $R^2(Q^{-1}) = 0.915$ and $R^2(E) = 0.932$.

The resulting inversion (Figure 13) shows only modest improvements in point-estimate recovery: the probability of correctly recovering the exponent a increases to roughly 30-40%, and that for the density d to about 50-60%. However, the top-two recovery probabilities remain essentially unchanged from Figure 10, indicating that posterior ambiguity persists despite removing $\tilde{\kappa}_{\text{obs}}$. This persistent ambiguity reflects an intrinsic information limit of the soft-fracture regime: when $\tilde{\kappa}$ is small, fracture network properties dominate the response and many different combinations of (a, d, p) produce nearly indistinguishable (Q^{-1}, E) pairs. Consequently, even a surrogate trained without $\tilde{\kappa}$ cannot fully resolve these degeneracies.

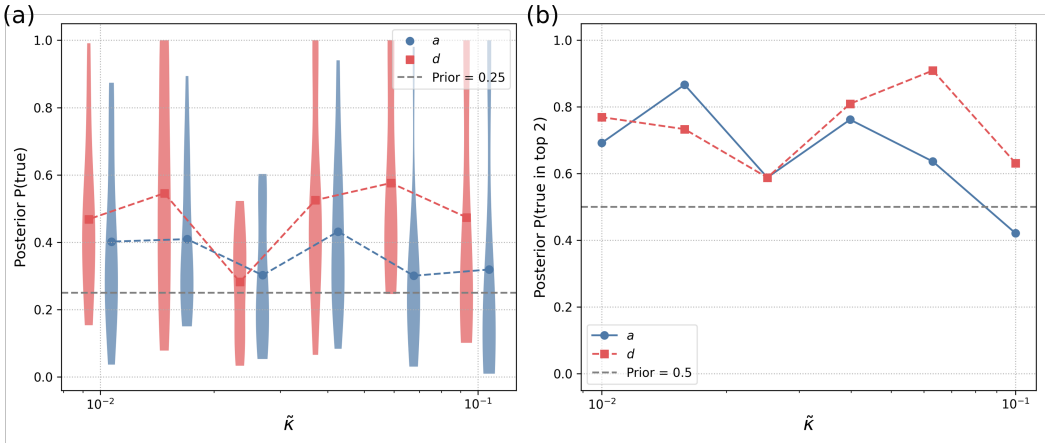

Figure 13. Inversion results in the soft-fracture band ($\tilde{\kappa} \leq 0.1$) when the stiffness constraint $\tilde{\kappa}_{\text{obs}}$ is omitted. **(a)** Mean recovery probability that MAP estimates $\hat{a}$, $\hat{d}$ equal the true values. **(b)** Probability that the true a or d lies in the two highest-probability posterior modes. The dashed lines mark the uniform prior baselines of 0.25 (a) and 0.5 (b).

Conceptually, the fracture network behaves as an ensemble of individual fractures whose collective interactions govern wavefield evolution. At large $\tilde{\kappa}$, the wave interacts with each fracture almost in isolation, so individual stiffness dominates attenuation. At small $\tilde{\kappa}$, the wave must navigate the entire network, so fracture network properties become the primary controls, leading to anomalous diffusion or localization. The sliding-window DGSA therefore provides a quantitative picture of how single-fracture stiffness and fracture network geometry jointly shape elastic-wave transport in fractured media, and explains why different stiffness regimes favor the identifiability of different subsets of parameters.

4.4 Limitations and Outlook

Several limitations of the present study point to directions for future work. First, we use a 2D elastic wave model that omits out-of-plane scattering and also does not reflect the full geometric complexity of 3D fracture networks. This approximation is best viewed as a plane-strain idealization, which is most appropriate for systems that are effectively invariant in the out-of-plane direction and where deformation in that direction is constrained. In general, the restriction to 2D suppresses out-of-plane scattering pathways, which reduces the number of available propagation channels and may therefore lead to an underestimation of scattering attenuation compared to fully 3D systems (Lei & Sornette, 2021, 2022). At the same time, 2D wavefields exhibit stronger recurrence and repeated in-plane interactions than 3D systems, which can enhance apparent trapping and localization within a finite domain (Abrahams et al., 1979; Lagendijk et al., 2009; Sheng & van Tiggelen, 2007). In addition, 2D fracture traces do not uniquely represent the connectivity state of finite-sized 3D fracture networks, whose percolation behavior can differ from that inferred from 2D patterns (Bour & Davy, 1998; Lang et al., 2014). The present 2D results are therefore used to mainly identify governing mechanisms, sensitivity hierarchies, and relative transitions between transport regimes, rather than to provide direct 3D predictions of absolute Q^{-1} values or regime thresholds. Dedicated 3D simulations remain necessary for a more complete representation of wave transport in 3D fractured media.

Second, all simulations use a fixed source wavelength ($\lambda = L/10$). In the present formulation, frequency-dependent effects are incorporated through the dimensionless fracture stiffness, whose inverse is equal to the dimensionless angular frequency (Lei & Sornette, 2021,

2022; Pyrak-Nolte et al., 1990). As a result, the parameter space explored in this study effectively spans a range of frequency-dependent responses, even though the wavelength itself is not varied explicitly. The use of a fixed wavelength is a deliberate choice to isolate the governing dimensionless control. Within this framework, wave–fracture interaction is governed not only by the geometric ratio between wavelength and fracture size, but by the combined effect of geometry and compliance captured by the dimensionless stiffness. In particular, fractures with sufficiently high stiffness become effectively transparent to the wavefield, even if their geometric size is large, whereas compliant fractures can induce strong scattering even at smaller scales. Previous studies have shown that attenuation and dispersion can depend on both compliance-related properties and the ratio between wavelength and the characteristic size of heterogeneities (Z. Wang, Wang, Li, et al., 2015; Z. Wang, Wang, Weger, et al., 2015). In the present framework, these effects are captured in a coupled manner through the dimensionless fracture stiffness. While multi-frequency analyses could provide complementary perspectives by varying wavelength independently, such variations would not fundamentally decouple fracture size from stiffness, as both enter the problem through the same dimensionless control.

Third, the present framework isolates scattering attenuation and does not consider intrinsic attenuation due to the effects of fluids within fractures or pores of fluid-bearing rocks (Pyrak-Nolte et al., 1990; Schoenberg, 1980). In particular, the presence of fluids can increase the apparent normal stiffness of fractures, while viscous and poroelastic processes can also introduce frequency-dependent attenuation and velocity dispersion that are physically distinct from elastic scattering. Pore-scale studies also show that wave dispersion depends on both pore structure and fluid properties, and may differ substantially between air-saturated and water-saturated cases (Z. Wang, Wang, Weger, et al., 2015). As a result, part of the response currently attributed to fracture intensity, fracture-size distribution, or the soft-fracture regime could, in natural fluid-bearing systems, also reflect fluid-related stiffening and damping. The soft-fracture regime identified here may therefore shift, broaden, or become less distinct once fluid effects are included. Extending the present framework toward coupled hydro-mechanical models is thus an important next step for testing how robust the current sensitivity and identifiability patterns remain under fluid-saturated subsurface conditions.

Fourth, we discretize the prior distributions of a and d into a finite set of levels and employ a random forest surrogate, which may introduce discretization effects in the posterior. Because the inversion is performed on a discretized parameter grid, some sharp posterior contrasts may partly reflect the imposed parameter levels rather than fully resolved physical separability. Future work could instead use surrogates defined on continuous parameter spaces, such as multi-fidelity Gaussian processes or physics-informed neural networks, and combine them with Bayesian experimental design (Thibaut et al., 2022, 2021). This would allow smoother posteriors, more explicit uncertainty estimates, and a closer link between inversion and survey design (Amaya et al., 2024; Rasht-Behesht et al., 2022).

Finally, attenuation-based inversion becomes less informative when the observations fall in the subdiffusion or localization regimes, where the responses of Q^{-1} and E tend to become insensitive to parameter variations. In such cases, complementary geophysical measurements may help constrain fracture network properties. For example, cross-well thermal tracer tests have been used to infer fracture connectivity and aperture, and electrical resistivity tomography has been applied to image fracture zones by mapping resistivity contrasts (de La Bernardie et al., 2018; Molron et al., 2020). Extending the metric set beyond Q^{-1} and E to include time-frequency attributes such as instantaneous frequency shifts, coda-decay exponents, and wavelet-based amplitude envelopes may also improve constraints on fracture parameters (Schisselé et al., 2004; W. Wang & Shearer, 2017).

5 Conclusions

This study has presented a sensitivity and inversion framework for inferring fracture properties based on elastic waves. By combining distance-based generalized sensitivity analysis (DGSA), a random forest surrogate, and a Metropolis-Hastings sampler, we showed that two simple wave transport metrics, the inverse quality factor Q^{-1} and the normalized transmitted energy E, carry valuable information to constrain key fracture network parameters: the length power-law exponent a, the fracture density d, the percolation parameter p, and, in suitable regimes, the dimensionless fracture stiffness $\tilde{\kappa}$.

The stiffness-dependent analysis identifies three wavefield regimes. For large $\tilde{\kappa}$ (propagation and superdiffusion), wave behavior is governed primarily by the individual fracture stiffness and $\tilde{\kappa}$ itself can be inferred, whereas the network parameters (a, d, p) are only moderately constrained. For intermediate $\tilde{\kappa}$ (normal diffusion), both individual fracture stiffness and fracture network properties control the wave energy transport, and both $\tilde{\kappa}$ and (a, d, p) can be recovered, with the best posterior recovery for a and especially d. For small $\tilde{\kappa}$ (subdiffusion and localization), fracture network properties dominate the wavefield evolution, sensitivity to $\tilde{\kappa}$ collapses and stiffness becomes poorly identifiable, while density and connectivity parameters retain information until strong localization is reached. Overall, the results indicate that simple wave transport metrics, used in the appropriate stiffness regime, can serve as practical observables for Bayesian inversion of fracture properties, and they provide guidance for designing and interpreting geophysical surveys of fractured geological formations.

Acknowledgments

This work was supported by the Bilateral Cooperation Project between Flanders and China (grant number G0E5222N). The authors thank the Editor Prof. Daniel O'Malley, the Associate Editor, and three anonymous referees for their constructive reviews that improved the manuscript.

Conflict of Interest Statement

The authors declare no conflicts of interest relevant to this study.

Data availability

The dataset supporting this study is archived on Zenodo at L. Zhang (2025).

Appendix A DGSA Mathematical Details

This appendix provides the detailed mathematical derivations and formulas for the DGSA approach used in Section 2.3.

A1 First-order Sensitivity Index

Initially, this method divides outputs into several clusters using a distance-based clustering approach. Let X be a model parameter and C the number of clusters. The normalized first-order sensitivity index is defined as (Park et al., 2016):

$$S(X) = \frac{1}{C}\sum_{c=1}^{C} \widehat{d}_c = \frac{1}{C}\sum_{c=1}^{C} \frac{d_{L1}\big(F(X),\, F(X \mid c)\big)}{\check{d}_a^c}, \tag{A1}$$

where

$$\widehat{d}_c = \frac{d_{L1}\big(F(X),\, F(X \mid c)\big)}{\check{d}_a^c}, \quad d_{L1}\big(F(X),\, F(X \mid c)\big) \;=\; \int \Big| F_X(x) - F_{X|c}(x) \Big|\, dx,$$

where $\check{d}_a^c$ is the ath quartile of the within-cluster distances for cluster c, with $a = 0.95$ adopted in this study. Here, $F(X)$ denotes the CDF of the parameter X over all samples, and $F(X \mid c)$ the CDF conditioned on the membership in cluster c. If $S(X) > 1$, parameter X is considered sensitive (Liu et al., 2026; Scheidt et al., 2018).

A2 Second-order (Conditional) Sensitivity Index

DGSA can also compute conditional (second-order) sensitivities to account for interactions between two parameters X_i and X_j. The conditional sensitivity $S(X_i \mid X_j)$ is given by:

$$S(X_i \mid X_j) = \frac{1}{C}\frac{1}{L}\sum_{c=1}^{C}\sum_{l=1}^{L} \widehat{d}_{c,i|j,l}, \tag{A2}$$

where

$$\widehat{d}_{c,i|j,l} = \frac{d_{L1}\big(F(X_i \mid j = l),\, F(X_i \mid c)\big)}{\widehat{\check{d}}_{c,i|j,l}(a)}, \quad l = 1, \ldots, L,\; c = 1, \ldots, C.$$

Here, $F(X_i \mid j = l)$ is the CDF of X_i given that X_j takes its lth level, and $\widehat{\check{d}}_{c,i|j,l}(a)$ denotes the ath quartile of the within-cluster distances for X_i in cluster c when X_j is fixed at level l.

References

Abrahams, E., Anderson, P. W., Licciardello, D. C., & Ramakrishnan, T. V. (1979). Scaling theory of localization: Absence of quantum diffusion in two dimensions. *Physical Review Letters*, *42*(10), 673. doi: 10.1103/PhysRevLett.42.673

Aki, K., & Richards, P. G. (2002). Quantitative seismology 2nd edn. *Herndon, VA: University Science Books*, 37–59.

Ali, A., & Jakobsen, M. (2011). Seismic characterization of reservoirs with multiple fracture sets using velocity and attenuation anisotropy data. *Journal of Applied Geophysics*, *75*(3), 590–602. doi: 10.1016/j.jappgeo.2011.09.003

Amaya, M., Meles, G., Marelli, S., & Linde, N. (2024). Multifidelity adaptive sequential monte carlo for geophysical inversion. *Geophysical Journal International*, *237*(2), 788–804.

Arendt, P. D., Apley, D. W., & Chen, W. (2012). Quantification of model uncertainty: Calibration, model discrepancy, and identifiability. *Journal of Mechanical Design*, *134*(10). doi: 10.1115/1.4007390

Arendt, P. D., Apley, D. W., Chen, W., Lamb, D., & Gorsich, D. (2012). Improving identifiability in model calibration using multiple responses. *Journal of Mechanical Design*, *134*(10), 101005. doi: 110.1115/1.4007573

Baird, A. F., Kendall, J.-M., & Angus, D. A. (2013). Frequency-dependent seismic anisotropy due to fractures: Fluid flow versus scattering. *Geophysics*, *78*(2), WA111–WA122. doi: 10.1190/geo2012-0288.1

Barbosa, N. D., Caspari, E., Rubino, J. G., Greenwood, A., Baron, L., & Holliger, K. (2019). Estimation of fracture compliance from attenuation and velocity analysis of full-waveform sonic log data. *Journal of Geophysical Research: Solid Earth*, *124*(3), 2738–2761. doi: 10.1029/2018JB016507

Ben-Zion, Y. (1998). Properties of seismic fault zone waves and their utility for imaging low-velocity structures. *Journal of Geophysical Research: Solid Earth*, *103*(B6), 12567–12585. doi: 10.1029/98JB00768

Ben-Zion, Y., & Malin, P. (1991). San andreas fault zone head waves near parkfield, california. *Science*, *251*(5001), 1592–1594. doi: 10.1126/science.251.5001.1592

Ben-Zion, Y., Peng, Z., Okaya, D., Seeber, L., Armbruster, J. G., Ozer, N., ... Aktar, M. (2003). A shallow fault-zone structure illuminated by trapped waves in the karadere–duzce branch of the north anatolian fault, western turkey. *Geophysical Journal International*, *152*(3), 699–717. doi: 10.1046/j.1365-246X.2003.01870.x

Berkowitz, B. (2002). Characterizing flow and transport in fractured geological media: A review. *Advances in water resources*, *25*(8-12), 861–884. doi: 10.1016/S0309-1708(02)00042-8

Bonnet, E., Bour, O., Odling, N. E., Davy, P., Main, I., Cowie, P., & Berkowitz, B. (2001). Scaling of fracture systems in geological media. *Reviews of geophysics*, *39*(3), 347–383. doi: 10.1029/1999RG000074

Bouchaud, J.-P., & Georges, A. (1990). Anomalous diffusion in disordered media: statistical mechanisms, models and physical applications. *Physics reports*, *195*(4-5), 127–293. doi: 10.1016/0370-1573(90)90099-N

Bour, O., & Davy, P. (1997). Connectivity of random fault networks following a power law fault length distribution. *Water Resources Research*, *33*(7), 1567–1583. doi: 10.1029/96WR00433

Bour, O., & Davy, P. (1998). On the connectivity of three-dimensional fault networks. *Water Resources Research*, *34*(10), 2611–2622. doi: 10.1029/98WR01861

Bour, O., Davy, P., Darcel, C., & Odling, N. (2002). A statistical scaling model for fracture network geometry, with validation on a multiscale mapping of a joint network (hornelen basin, norway). *Journal of Geophysical Research: Solid Earth*, *107*(B6), ETG–4. doi: 10.1029/2001JB000176

Chen, Y., Voskov, D., & Daniilidis, A. (2025). Rigorous numerical methodology and heat recovery analysis for modeling of direct use geothermal systems. *Geoenergy Science and Engineering*, *247*, 213661. doi: 10.1016/j.geoen.2025.213661

Darcel, C., Bour, O., Davy, P., & De Dreuzy, J. (2003). Connectivity properties of two-dimensional fracture networks with stochastic fractal correlation. *Water resources research*, *39*(10). doi: 10.1029/2002WR001628

Davy, P., Le Goc, R., Darcel, C., Bour, O., de Dreuzy, J.-R., & Munier, R. (2010). A likely universal model of fracture scaling and its consequence for crustal hydromechanics. *Journal of Geophysical Research: Solid Earth*, *115*(B10). doi: 10.1029/2009JB007043

de La Bernardie, J., Bour, O., Le Borgne, T., Guihéneuf, N., Chatton, E., Labasque, T., ... Gerard, M.-F. (2018). Thermal attenuation and lag time in fractured rock: Theory and field measurements from joint heat and solute tracer tests. *Water Resources Research*, *54*(12), 10–053. doi: 10.1029/2018WR023199

Frankel, A., & Clayton, R. W. (1986). Finite difference simulations of seismic scattering: Implications for the propagation of short-period seismic waves in the crust and models of crustal heterogeneity. *Journal of Geophysical Research: Solid Earth*, *91*(B6), 6465–6489. doi: 10.1029/JB091iB06p06465

Gelman, A., & Rubin, D. B. (1992). Inference from iterative simulation using multiple sequences. *Statistical science*, *7*(4), 457–472. doi: 10.1214/ss/1177011136

Germán Rubino, J., Guarracino, L., Müller, T. M., & Holliger, K. (2013). Do seismic waves sense fracture connectivity? *Geophysical Research Letters*, *40*(4), 692–696. doi: 10.1002/grl.50127

Germán Rubino, J., Müller, T. M., Guarracino, L., Milani, M., & Holliger, K. (2014). Seismoacoustic signatures of fracture connectivity. *Journal of Geophysical Research: Solid Earth*, *119*(3), 2252–2271. doi: 10.1002/2013JB010567

Graff, K. (1991). *Wave motion in elastic solids*. Dover Publications.

Hermans, T., Lesparre, N., De Schepper, G., & Robert, T. (2019). Bayesian evidential

learning: a field validation using push-pull tests. *Hydrogeology Journal*, *27*(5), 1661–1672. doi: 10.1007/s10040-019-01962-9

Hermans, T., Nguyen, F., Klepikova, M., Dassargues, A., & Caers, J. (2018). Uncertainty quantification of medium-term heat storage from short-term geophysical experiments using bayesian evidential learning. *Water Resources Research*, *54*(4), 2931–2948. doi: 10.1002/2017wr022135

Hermans, T., Oware, E., & Caers, J. (2016). Direct prediction of spatially and temporally varying physical properties from time-lapse electrical resistance data. *Water Resources Research*, *52*(9), 7262–7283. doi: 10.1002/2016WR019126

Hillers, G., Campillo, M., Ben-Zion, Y., & Roux, P. (2014). Seismic fault zone trapped noise. *Journal of Geophysical Research: Solid Earth*, *119*(7), 5786–5799. doi: 10.1002/2014JB011217

Hudson, J., Liu, E., & Crampin, S. (1996). Transmission properties of a plane fault. *Geophysical Journal International*, *125*(2), 559–566. doi: 10.1111/j.1365-246X.1996.tb00018.x

Hudson, J., Liu, E., & Crampin, S. (1997). The mean transmission properties of a fault with imperfect facial contact. *Geophysical Journal International*, *129*(3), 720–726. doi: 10.1111/j.1365-246X.1997.tb04507.x

Hudson, J. A., & Liu, E. (1999). Effective elastic properties of heavily faulted structures. *Geophysics*, *64*(2), 479–485. doi: 10.1190/1.1444553

Hunziker, J., Favino, M., Caspari, E., Quintal, B., Rubino, J. G., Krause, R., & Holliger, K. (2018). Seismic attenuation and stiffness modulus dispersion in porous rocks containing stochastic fracture networks. *Journal of Geophysical Research: Solid Earth*, *123*(1), 125–143. doi: 10.1002/2017JB014566

Jia, H., Xu, T., Liang, S., Zhao, P., & Xu, C. (2018). Bayesian framework of parameter sensitivity, uncertainty, and identifiability analysis in complex water quality models. *Environmental Modelling & Software*, *104*, 13–26. doi: 10.1016/j.envsoft.2018.03.001

Lagendijk, A., Tiggelen, B. v., & Wiersma, D. S. (2009). Fifty years of anderson localization. *Physics today*, *62*(8), 24–29. doi: 10.1063/1.3206091

Lang, P., Paluszny, A., & Zimmerman, R. W. (2014). Permeability tensor of three-dimensional fractured porous rock and a comparison to trace map predictions. *Journal of Geophysical Research: Solid Earth*, *119*(8), 6288–6307. doi: 10.1002/2014JB011027

Lei, Q. (2022). Impact of fracture normal and shear stiffnesses on the scattering attenuation of p and s waves in a naturally fractured rock. *Journal of Applied Geophysics*, *206*, 104784. doi: 10.1016/j.jappgeo.2022.104784

Lei, Q., & Gao, K. (2018). Correlation between fracture network properties and stress variability in geological media. *Geophysical Research Letters*, *45*(9), 3994–4006. doi: 10.1002/2018GL077548

Lei, Q., Latham, J.-P., Tsang, C.-F., Xiang, J., & Lang, P. (2015). A new approach to upscaling fracture network models while preserving geostatistical and geomechanical characteristics. *Journal of Geophysical Research: Solid Earth*, *120*(7), 4784–4807. doi: 10.1002/2014JB011736

Lei, Q., & Sornette, D. (2021). Transport and localization of elastic waves in two-dimensional fractured media: Consequences on scattering attenuation. *Journal of Geophysical Research: Solid Earth*, *126*(6), e2020JB021178. doi: 10.1029/2020JB021178

Lei, Q., & Sornette, D. (2022). Anderson localisation and reentrant delocalisation of tensorial elastic waves in two-dimensional fractured media. *Europhysics Letters*, *136*(3), 39001. doi: 10.1209/0295-5075/ac225d

Lewis, M. A., & Ben-Zion, Y. (2010). Diversity of fault zone damage and trapping structures in the parkfield section of the san andreas fault from comprehensive analysis of near fault seismograms. *Geophysical Journal International*, *183*(3), 1579–1595. doi: 10.1111/j.1365-246X.2010.04816.x

Liu, L., Shi, M., Elsworth, D., Wang, T., Ji, H., Zhang, L., & Li, Y. (2026). Coupled tm-damage modeling and global sensitivity analysis of thermal spalling in heterogeneous rocks. *International Journal of Mining Science and Technology*. doi: 10.1016/j.ijmst.2026.01.008

Maultzsch, S., Chapman, M., Liu, E., & Li, X. Y. (2003). Modelling frequency-dependent seismic anisotropy in fluid-saturated rock with aligned fractures: implication of fracture size estimation from anisotropic measurements. *Geophysical Prospecting*, *51*(5), 381–392. doi: 10.1046/j.1365-2478.2003.00386.x

Molron, J., Linde, N., Baron, L., Selroos, J.-O., Darcel, C., & Davy, P. (2020). Which fractures are imaged with ground penetrating radar? results from an experiment in the äspö hardrock laboratory, sweden. *Engineering geology*, *273*, 105674. doi: 10.1016/j.enggeo.2020.105674

Park, J., Yang, G., Satija, A., Scheidt, C., & Caers, J. (2016). Dgsa: A matlab toolbox for distance-based generalized sensitivity analysis of geoscientific computer experiments. *Computers & geosciences*, *97*, 15–29. doi: 10.1016/j.cageo.2016.08.021

Pettit, J., Walker, A., Cawley, P., & Lowe, M. (2014). A stiffness reduction method for efficient absorption of waves at boundaries for use in commercial finite element codes. *Ultrasonics*, *54*(7), 1868–1879. doi: 10.1016/j.ultras.2013.11.013

Pyrak-Nolte, L. J. (1996). The seismic response of fractures and the interrelations among fracture properties. In *International journal of rock mechanics and mining sciences & geomechanics abstracts* (Vol. 33, pp. 787–802). doi: 10.1016/S0148-9062(96)00022-8

Pyrak-Nolte, L. J., & Cook, N. G. (1987). Elastic interface waves along a fracture. *Geophysical Research Letters*, *14*(11), 1107–1110. doi: 10.1029/GL014i011p01107

Pyrak-Nolte, L. J., Myer, L. R., & Cook, N. G. (1990). Transmission of seismic waves across single natural fractures. *Journal of Geophysical Research: Solid Earth*, *95*(B6), 8617–8638. doi: 10.1029/JB095iB06p08617

Pyrak-Nolte, L. J., & Nolte, D. D. (1995). Wavelet analysis of velocity dispersion of elastic interface waves propagating along a fracture. *Geophysical Research Letters*, *22*(11), 1329–1332. doi: 10.1029/95GL01323

Pyrak-Nolte, L. J., Xu, J., & Haley, G. M. (1992). Elastic interface waves propagating in a fracture. *Physical review letters*, *68*(24), 3650. doi: 10.1103/PhysRevLett.68.3650

Rasht-Behesht, M., Huber, C., Shukla, K., & Karniadakis, G. E. (2022). Physics-informed neural networks (pinns) for wave propagation and full waveform inversions. *Journal of Geophysical Research: Solid Earth*, *127*(5), e2021JB023120. doi: 10.1029/2021JB023120

Scheidt, C., Li, L., & Caers, J. (2018). *Quantifying uncertainty in subsurface systems* (Vol. 236). John Wiley & Sons. doi: 10.1002/9781119325888.ch8

Schisselé, E., Guilbert, J., Gaffet, S., & Cansi, Y. (2004). Accurate time-frequency-wavenumber analysis to study coda waves. *Geophysical Journal International*, *158*(2), 577–591. doi: 10.1111/j.1365-246X.2004.02211.x

Schoenberg, M. (1980). Elastic wave behavior across linear slip interfaces. *The Journal of the Acoustical Society of America*, *68*(5), 1516–1521. doi: 10.1121/1.385077

Sheng, P., & van Tiggelen, B. (2007). *Introduction to wave scattering, localization and mesoscopic phenomena.* Taylor & Francis. doi: 10.1080/17455030701219165

Smith, T. J., & Marshall, L. A. (2008). Bayesian methods in hydrologic modeling: A study of recent advancements in markov chain monte carlo techniques. *Water Resources Research*, *44*(12). doi: 10.1029/2007WR006705

Tas, L., Caers, J., & Hermans, T. (2025). Decision-making under uncertainty for lt-ates systems in complex subsurface settings: application to a low-transmissivity aquifer. *Advances in Water Resources*, 105193. doi: 10.1016/j.advwatres.2025.105193

Tas, L., Hartog, N., Bloemendal, M., Simpson, D., Robert, T., Thibaut, R., ... Hermans, T. (2025). Efficiency and heat transport processes of low-temperature aquifer thermal energy storage systems: new insights from global sensitivity analyses. *Geothermal Energy*, *13*(1), 1–27. doi: 10.1186/s40517-024-00326-1

Thibaut, R., Compaire, N., Lesparre, N., Ramgraber, M., Laloy, E., & Hermans, T. (2022). Comparing well and geophysical data for temperature monitoring within a bayesian experimental design framework. *Water Resources Research*, *58*(11), e2022WR033045. doi: 10.1029/2022WR033045

Thibaut, R., Laloy, E., & Hermans, T. (2021). A new framework for experimental design using bayesian evidential learning: The case of wellhead protection area. *Journal of*

Hydrology, *603*, 126903. doi: 10.1016/j.jhydrol.2021.126903

Tsang, C.-F. (1999). Linking thermal, hydrological, and mechanical processes in fractured rocks. *Annual review of earth and planetary sciences*, *27*(1), 359–384. doi: 10.1146/annurev.earth.27.1.359

Virieux, J., & Operto, S. (2009). An overview of full-waveform inversion in exploration geophysics. *Geophysics*, *74*(6), WCC1–WCC26. doi: 10.1190/1.3238367

Viswanathan, H. S., Ajo-Franklin, J., Birkholzer, J. T., Carey, J. W., Guglielmi, Y., Hyman, J., ... others (2022). From fluid flow to coupled processes in fractured rock: Recent advances and new frontiers. *Reviews of Geophysics*, *60*(1), e2021RG000744. doi: 10.1029/2021RG000744

Wang, K., Peng, S., Lu, Y., & Cui, X. (2021). Full waveform inversion in fractured media based on velocity–stress wave equations in the time domain. *Geophysical Journal International*, *227*(2), 1060–1075. doi: 10.1093/gji/ggab243

Wang, W., & Shearer, P. (2017). Using direct and coda wave envelopes to resolve the scattering and intrinsic attenuation structure of southern california. *Journal of Geophysical Research: Solid Earth*, *122*(9), 7236–7251. doi: 10.1002/2016JB013810

Wang, Z., Wang, R., Li, T., Qiu, H., & Wang, F. (2015). Pore-scale modeling of pore structure effects on p-wave scattering attenuation in dry rocks. *PloS one*, *10*(5), e0126941. doi: 10.1371/journal.pone.0126941

Wang, Z., Wang, R., Weger, R. J., Li, T., & Wang, F. (2015). Pore-scale modeling of elastic wave propagation in carbonate rocks. *Geophysics*, *80*(1), D51–D63. doi: 10.1190/GEO2014-0050.1

Wu, X., Shirvan, K., & Kozlowski, T. (2019). Demonstration of the relationship between sensitivity and identifiability for inverse uncertainty quantification. *Journal of computational physics*, *396*, 12–30. doi: 10.1016/j.jcp.2019.06.032

Xu, T., Valocchi, A. J., Ye, M., & Liang, F. (2017). Quantifying model structural error: Efficient b ayesian calibration of a regional groundwater flow model using surrogates and a data-driven error model. *Water Resources Research*, *53*(5), 4084–4105. doi: 10.1002/2016WR019831

Yang, J., Zhu, H., Li, X., Ren, L., & Zhang, S. (2020). Estimating p wave velocity and attenuation structures using full waveform inversion based on a time domain complex-valued viscoacoustic wave equation: The method. *Journal of Geophysical Research: Solid Earth*, *125*(6), e2019JB019129. doi: 10.1029/2019JB019129

Zhang, J., Zheng, Q., Chen, D., Wu, L., & Zeng, L. (2020). Surrogate-based bayesian inverse modeling of the hydrological system: An adaptive approach considering surrogate approximation error. *Water Resources Research*, *56*(1), e2019WR025721. doi: 10.1029/2019WR025721

Zhang, L. (2025). *Surrogate-assisted bayesian inversion of fracture network parameters from elastic waves [data set]*. Zenodo. doi: 10.5281/zenodo.17968358

Zhang, L., Daniilidis, A., Dieudonné, A.-C., Thibaut, R., & Hermans, T. (2026). A bayesian evidential learning framework for safety and performance prediction in thermo-hydro-mechanical coupled deep mine geothermal systems. *Journal of Rock Mechanics and Geotechnical Engineering*. doi: 10.1016/j.jrmge.2025.11.022

Zhang, L., Dieudonné, A.-C., Daniilidis, A., Dong, L., Cao, W., Thibaut, R., ... Hermans, T. (2025). Thermo-hydro-mechanical modeling of geothermal energy systems in deep mines: uncertainty quantification and design optimization. *Applied Energy*, *377*, 124531. doi: 10.1016/j.apenergy.2024.124531

Zhang, L., Mi, Z., Cao, W., Liu, L., Tas, L., & Hermans, T. (2025). Multi-objective optimization of energy efficiency and geomechanical safety in high-temperature aquifer thermal energy storage (ht-ates) systems based on coupled thermo-hydro-mechanical (thm) analysis. *Energy*, 137096. doi: 10.1016/j.energy.2025.137096